Mon. Not. R. Astron. Soc. **334,** 401–418 (2002)

Radiation from the first forming stars

E. Ripamonti,[1]★ F. Haardt,[2] A. Ferrara[3] and M. Colpi[4]
[1]*Università degli Studi di Milano, Dipartimento di Fisica, Via Celoria 16, 20133 Milano, Italy*
[2]*Università dell'Insubria, Dipartimento di Scienze Chimiche Fisiche e Matematiche, Via Valleggio 11, 22100 Como, Italy*
[3]*Osservatorio Astrofisico di Arcetri, Largo Enrico Fermi 5, 50125 Firenze, Italy*
[4]*Università degli Studi Milano-Bicocca, Dipartimento di Fisica G. Occhialini, Piazza delle Scienze 3, 20126 Milano, Italy*

Accepted 2002 March 21. Received 2002 January 30; in original form 2001 July 9

ABSTRACT

The evolution of radiation emitted during the dynamical collapse of metal-free protostellar clouds is investigated within a spherically symmetric hydrodynamical scheme that includes the transfer of radiation and the chemistry of the primordial gas. The cloud centre collapses on a time-scale of $\sim 10^{5-6}$ yr, thanks to line cooling from molecular hydrogen (H_2). For most of the collapse time, when the evolution proceeds self-similarly, the luminosity slowly rises up to $\sim 10^{36}$ erg and is essentially a result of H_2 infrared (IR) line emission. Later, continuum IR radiation provides an additional contribution, which is mostly a result of the accretion of an infalling envelope upon a small hydrostatic protostellar core that develops in the centre. We follow the beginning of the accretion phase, when the enormous accretion rate ($\sim 0.1\,M_\odot\,yr^{-1}$) produces a very high continuum luminosity of $\sim 10^{36}$ erg. Despite the high luminosities, the radiation field is unable to affect the gas dynamics during the collapse and the first phases of accretion, because the opacity of the infalling gas is too small; this is quite different from present-day star formation. We also find that the protostellar evolution is similar among clouds with different initial configurations, including those resulting from three-dimensional cosmological simulations of primordial objects; in particular, the shape of the molecular spectra is quite universal. Finally, we briefly discuss the detectability of this initial cosmic star formation activity.

Key words: stars: formation – stars: luminosity function, mass function – Galaxy: formation – cosmology: theory.

1 INTRODUCTION

As the temperature of the cosmic bath decreases, atoms start to recombine and therefore decouple from the cosmic microwave background (CMB) radiation at redshift ≈ 1100. The baryonic Jeans mass immediately after this event is given by

$$M_J \simeq 4.5 \times 10^4 \left(\frac{\Omega_b}{\Omega}\right)(\Omega h^2)^{-1/2}\,M_\odot, \quad (1)$$

where Ω and Ω_b are the matter and baryon density parameters, respectively. Masses larger than M_J are gravitationally unstable and should, in principle, collapse. However, in order for the actual collapse to occur a more severe condition must be satisfied, i.e. that the cooling time of the gas is shorter than the Hubble time at that epoch. In fact, radiative losses provide the only way for the gas to lose pressure and settle down in the potential well of the host dark matter halo. Since the virial temperature corresponding to the masses of the first objects (population III, hereafter PopIII) is typically $\lesssim 8000$ K, cooling by hydrogen Lyα excitation is strongly quenched, and the only viable coolant in a primordial H–He plasma is molecular hydrogen. H_2 is produced during the recombination phase, but its relic abundance is very small ($f_{H_2} \approx 10^{-6}$). This primordial fraction is usually lower than that required to fulfil the above time-scale constraint, but during the collapse phase the molecular hydrogen abundance reaches values that are high enough to allow the collapse to continue. It follows that the fate of a virialized lump depends crucially on its ability to rapidly increase its H_2 content during the collapse phase.

Haiman, Thoul & Loeb (1996) and Tegmark et al. (1997) have addressed this question by calculating the evolution of the H_2 abundance for different halo masses and initial conditions for a standard cold dark matter (CDM) cosmology. They conclude that if the prevailing conditions are such that a molecular hydrogen fraction of the order of $f_{H_2} \approx 5 \times 10^{-4}$ can be produced during the collapse, then the lump will cool, fragment and eventually form stars. This criterion is met only by the largest PopIIIs, implying that at each virialization redshift one can define a critical mass, M_{crit},

★E-mail: emanuele.ripamonti@mib.infn.it

such that only protogalaxies with total mass $M > M_{\rm crit}$ will be able to eventually form stars. As an example, a 3σ fluctuation of a cold dark matter primordial spectrum, has $M_{\rm crit} \approx 10^6\,{\rm M}_\odot$ and collapses at $z \approx 30$. Other studies have revised the value of $M_{\rm crit}$ as a result of a more accurate treatment of the microphysics (Nishi & Susa 1999; Fuller & Couchman 2000; Machacek, Bryan & Abel 2001); however, these results do not qualitatively alter the basic argument given above.

Recently, some works have started to tackle the formation and collapse of PopIII objects through numerical simulations (Abel et al. 1998; Nakamura & Umemura 1999, 2001; Bromm, Coppi & Larson 1999, 2002, 2002, hereafter BCL02; Abel, Bryan & Norman 2000, hereafter ABN00) based on hierarchical scenarios of structure formation. These studies have shown that gravitational collapse induces fragmentation of the first pre-galactic objects with initial baryonic mass $\approx 10^5\,{\rm M}_\odot$ into smaller clumps of typical mass $\sim 10^{2-3}\,{\rm M}_\odot$, which corresponds to the Jeans mass set by molecular hydrogen cooling.

Tracking the subsequent evolution of these clumps is a very challenging problem as it requires the simultaneous solution of the hydrodynamic equations and of radiative transfer in lines. At present, owing to the tremendous computational demand, this has only been possible in one-dimensional formulations of the problem. Star formation in the early universe naively appears to be easier to understand compared with the present, because several complicating effects can be neglected to a first approximation: among these are magnetic fields, dust grains and metal enrichment.

In their pioneering work, Omukai & Nishi (1998) (ON98) showed that at a certain stage of the collapse a quasi-hydrostatic central core is formed, the specific mass of which is almost independent on the details of the problem, with a typical value of $\sim 5 \times 10^{-3}\,{\rm M}_\odot$. However, as the accretion rate of the infalling gas is found to be rather high, around $10^{-2}\,{\rm M}_\odot\,{\rm yr}^{-1}$, the core mass at its formation might be unimportant in setting the final mass of the star. In the absence of any effect quenching accretion, a large fraction of the initial object can soon become part of the protostar. Pushing this conclusion a bit further, one might predict a top-heavy initial mass function (IMF) for this first generation of sources.

If the infall can instead be stopped, different scenarios can be envisaged. It has yet to be firmly established whether standard mechanisms proposed to halt the infall continue to work under primordial conditions: the radiation force might be opacity limited; bipolar flows need some magnetohydrodynamics (MHD) acceleration process and therefore seem to be excluded by the weak magnetic field present at the main formation epoch (Gnedin, Ferrara & Zweibel 2000), although the magnetic field could be amplified during the protostar formation process. An angular momentum barrier related to disc formation and competitive accretion among different clumps are slightly more promising, but much more difficult to model accurately. The estimate of the first mechanism (radiation reaction) requires one to accurately derive the properties of the radiation field produced during the collapse and to evaluate the effects of the radiation force on the infalling envelope. This is one of the main aims of the present paper.

The second motivation for our study consists in assessing the detection chances of distant PopIII objects via the (infrared) radiation they release during the collapse phase. Ciardi & Ferrara (2001) have already pointed out that IR H_2 molecular lines produced by the cooling of supernova-shocked PopIII gas are very likely to be observed by the *Next Generation Space Telescope*. However, as H_2 roto-vibrational lines are essentially the only carrier of the entire gravitational energy release, it seems worthwhile to compute the intensity, shape and evolution of the emitted spectrum in detail. Recently, Kamaya & Silk (2002, hereafter KS02) have estimated the H_2 luminosity from primordial collapsing stars using a very approximate treatment.

To investigate the described problem we have performed 1D numerical simulations, including a detailed treatment of the molecular line radiative transfer. The study is germane to that of ON98 but it includes the radiative force term in the dynamical equations adding a number of improvements, as we outline throughout the paper.

This paper is organized as follows. In Section 2, we present our numerical methodology. The choice and justification for the initial conditions, and the results of the simulation are discussed in Section 3. In Section 4 we discuss the luminosities and the detectability, and in the final section we give a brief summary.

2 NUMERICAL METHODS: THE CODE

We developed a 1D Lagrangian hydrodynamical code, including full treatment of radiative transfer and chemical evolution (with a careful treatment of the H_2 molecule, which is the main coolant in the initial phases of the collapse). Such code is similar to that described by ON98. Here we only summarize the relevant differences between the two; a more detailed description is given in the Appendix.

2.1 Dynamics: radiative force

We included the radiative force term into the momentum equation, which then becomes

$$\frac{{\rm d}v}{{\rm d}t} = -4\pi r^2 \frac{{\rm d}p}{{\rm d}M_{\rm r}} - \frac{GM_r}{r^2} + f_{\rm rad}, \tag{2}$$

where we are exploiting the spherical symmetry, and where

$$f_{\rm rad} = \frac{1}{c}\int \kappa_\nu F_\nu \, {\rm d}\nu \tag{3}$$

is the radiative force per unit mass, F_ν is the specific energy flux at frequency ν (both $f_{\rm rad}$ and F_ν are considered in the radial outward direction) and κ_ν is the opacity at frequency ν.

2.2 Chemistry and thermodynamics: non-ideal effects

As discussed by several authors (e.g. Hummer & Mihalas 1988; Mihalas, Däppen & Hummer 1988; Saumon, Chabrier & Van Horn 1995, hereafter SCVH95), at high densities ($\rho \gtrsim 10^{-3}\,{\rm g\,cm^{-3}}$) particles are jammed closely together, and the bound electron orbitals filling too large a volume fail to survive so that electrons migrate from atom to atom. Such an effect is known as *pressure ionization* and generally it is not taken into account in the Saha equations. As an example, a pure hydrogen gas with $\rho = 1\,{\rm g\,cm^{-3}}$ and $T = 3 \times 10^4\,{\rm K}$ is largely ionized (the mean distance between nuclei is only twice the Bohr radius of an H atom in its ground state, and the electrons are free in a Fermi gas, interacting simultaneously with several ions), while solving the Saha equations results in a completely molecular gas, which is clearly unphysical. In such regimes, the gas is also non-ideal, and the perfect gas equations are poor approximations.

For these reasons, at high densities and temperatures we find the chemical abundances and thermodynamical properties (such as the pressure p, the internal energy per unit mass u and the entropy

per unit mass s) by interpolation of the values tabulated by SCVH95, which are calculated using the *free-energy minimization* technique. The calculations of SCVH95 include several non-ideal effects, such as: (i) partial electron degeneracy; (ii) Coulomb interactions among charged particles; (iii) finite extension of 'hard-sphere' particles; (iv) weak attractive interactions (e.g. van der Waals); and (v) modifications of the internal partition functions owing to the shift of the energy levels.

3 THE SIMULATIONS

3.1 Initial conditions

The main parameters specifying the initial conditions of our runs are: the total cloud mass $M_{\rm tot}$, the temperature, density and velocity profiles $T_0(M_r)$, $\rho_0(M_r)$, $v_0(M_r)$, respectively, and the hydrogen molecular fraction $f_{\rm H_2}$.

Several previous investigations have set constraints on such parameters. Theoretical predictions of the mass of fragments leading to the birth of the first stars are quite uncertain, ranging from a minimum of $\sim 0.1\,{\rm M}_\odot$ (Palla, Salpeter & Stahler 1983), to $\gtrsim 200\,{\rm M}_\odot$ (Hutchins 1976). On the other hand, there is agreement concerning the value of $f_{\rm H_2} \sim 5 \times 10^{-4}$ and the value of $T_0(M_r)$, which is of the order of few hundred kelvin (e.g. Tegmark et al. 1997). Detailed numerical simulations (BCL02; ABN00) suggest that the runaway collapse starts soon after the (number) density reaches a value of 10^4–$10^5\,{\rm cm}^{-3}$. Such a value is determined by the transition from non-local thermodynamic equilibrium (non-LTE) cooling (with $\Lambda \propto n^2$) to LTE cooling (with $\Lambda \propto n$), slowing down the contraction, and allowing the gas to reach a quasi-hydrostatic state. This transition occurs when $T \sim 300$–$400\,{\rm K}$ and $f_{\rm H_2} \sim 5$–10×10^{-4}, inside a cloud with a mass of a few thousand ${\rm M}_\odot$, a value that is close to the Jeans mass of the cloud.

To check how our results depend on the choice of the initial conditions, we run a set of models with different initial masses $M_{\rm tot}$, ranging from 10 to $\sim 1500\,{\rm M}_\odot$. We use a constant profile for the H_2 abundance and zero velocity (the cloud is at rest). The density and temperature profiles inside the cloud are derived by imposing hydrostatic equilibrium and a polytropic index equal to 5/3 or 1 (isothermal). In addition we have considered 'numerical' profiles as given by ABN00 from cosmological simulations. In runs P10, owing to the high value of the initial central density, we used a higher value for $f_{\rm H_2}$. The initial electron fraction adopted is $f_{\rm e^-} = 10^{-10}$. With the exception of run P100/2, we always divide our simulated cloud into 100 Lagrangian shells, with massive external shells and much lighter internal ones (e.g. in run P100 each external shell comprises $\gtrsim 1\,{\rm M}_\odot$ of gas, while the central one has a mass of only $3 \times 10^{-7}\,{\rm M}_\odot$). Such a choice allows the fast evolution of the centre of the cloud, which only accounts for a tiny fraction of the total mass, to be followed with good resolution. Details of the initial conditions and general set up are given in Table 1. Note that runs P100 and P10 are directly comparable to those of ON98. Run P100/2 is identical to run P100, but the object is divided into 140 (rather than 100) shells; the 'extra' shells were used to improve the resolution in the particularly important region where the shock forms ($-3 \lesssim \log M_r \lesssim -1$).

Table 1. Initial conditions.

Run	$\rho_{0,\rm c}$ ($m_{\rm H}\,{\rm cm}^{-3}$)	$T_{0,\rm c}$ (K)	$f_{\rm H_2}$ (10^{-4})	Notes
P100	2.6×10^6	270	5	Cfr. ON98(A,B)
P100/2	2.6×10^6	270	5	Refinement of P100 (140 shells)
P1000	2.3×10^4	246	5	
P10	3.5×10^8	249	50	Cfr. ON98(C)
I100	7.8×10^7	300	5	
I1000	1.1×10^7	300	5	
N1500	2.0×10^6	440	5	From ABN00

The letter in the label of each run gives the assumed initial temperature/density profile: polytropic, isothermal (I), and numerical (N), i.e. after ABN00 results. It is followed by a number that gives the assumed total cloud mass $M_{\rm tot}$, in solar masses.

3.2 Dynamical evolution

The dynamics of the collapse is illustrated in Fig. 1, which shows the evolution of the cloud in run P100/2 at 10 different stages (see Table 2). In Figs 2 and 3 we show the evolution of the temperature and of the main hydrogen species in the most central shell as a function of density. In the rest of this section we will describe the results obtained in run P100/2 – the results of other runs are quite similar. In runs P100, P100/2 and P10 we find good agreement with the results of ON98.

In the beginning, the evolution is very well described by a Larson–Penston self-similar solution (Larson 1969, hereafter L69; Penston 1969) with a density profile scaling as $\rho \propto r^{-\alpha}$ (with $\alpha \simeq 2.2$). The self-similar evolution breaks down between stages 6 and 7, when a quasi-hydrostatic core forms in the centre and starts to grow in mass.

3.2.1 *The collapse phase*

During collapse the central regions of the cloud undergo several important chemical and thermal transformations. When the number density reaches $\gtrsim 10^8\,{\rm cm}^{-3}$ (stage 1), three-body reactions become efficient, converting the bulk of H into H_2 (Fig. 1, stages 2 and 3; Fig. 3). The growing H_2 fraction increases the gas cooling rate, only partially counterbalanced by radiative transfer effects (see Section 3.3). The evolution of the thermal properties of the gas is shown in Fig. 4, where the adiabatic heating $\Gamma_{\rm ad}$, the radiative cooling rate $\Lambda_{\rm rad}$ and the effective heating $\Gamma_{\rm eff} = \Gamma_{\rm ad} + \Gamma_{\rm ch}$ ($\Gamma_{\rm ch}$ is the heating, or cooling, caused by chemical reactions) are plotted versus the gas temperature. All of these quantities refer to the central shell. As $T \lesssim 1550\,{\rm K}$, the chemical heating arising from the H_2 formation dominates over $\Gamma_{\rm ad}$ and the heating and cooling terms almost balance, leading to a very slow temperature growth. For $T \gtrsim 1550\,{\rm K}$ H_2 is destroyed rather than formed, and the chemical term becomes a net cooling (this is the reason why the curves $\Gamma_{\rm eff}$ and $\Gamma_{\rm ad}$ cross at $T \simeq 1550\,{\rm K}$). At this stage the chemical and radiative cooling terms are of the same order. Radiative cooling is dominated by line radiation for $T \lesssim 1800\,{\rm K}$, while continuum emission is important above this temperature. However, continuum radiative cooling soon becomes highly inefficient because of the large optical depth: for $T \gtrsim 2350\,{\rm K}$ the innermost regions become almost adiabatic, and compressional heating is only matched by chemical cooling.

We just mentioned that H_2 starts to dissociate when $T \gtrsim 1550\,{\rm K}$. This process is slow because of the density increase and the chemical cooling associated with the dissociation process (4.48 eV per dissociated molecule is lost from the gas thermal energy). As a result, the H_2 fraction at the end of the self-similar phase ($T_{\rm c} \sim 15\,000\,{\rm K}$, stage 6) is still $\simeq 5$ per cent, even in the hottest central regions.

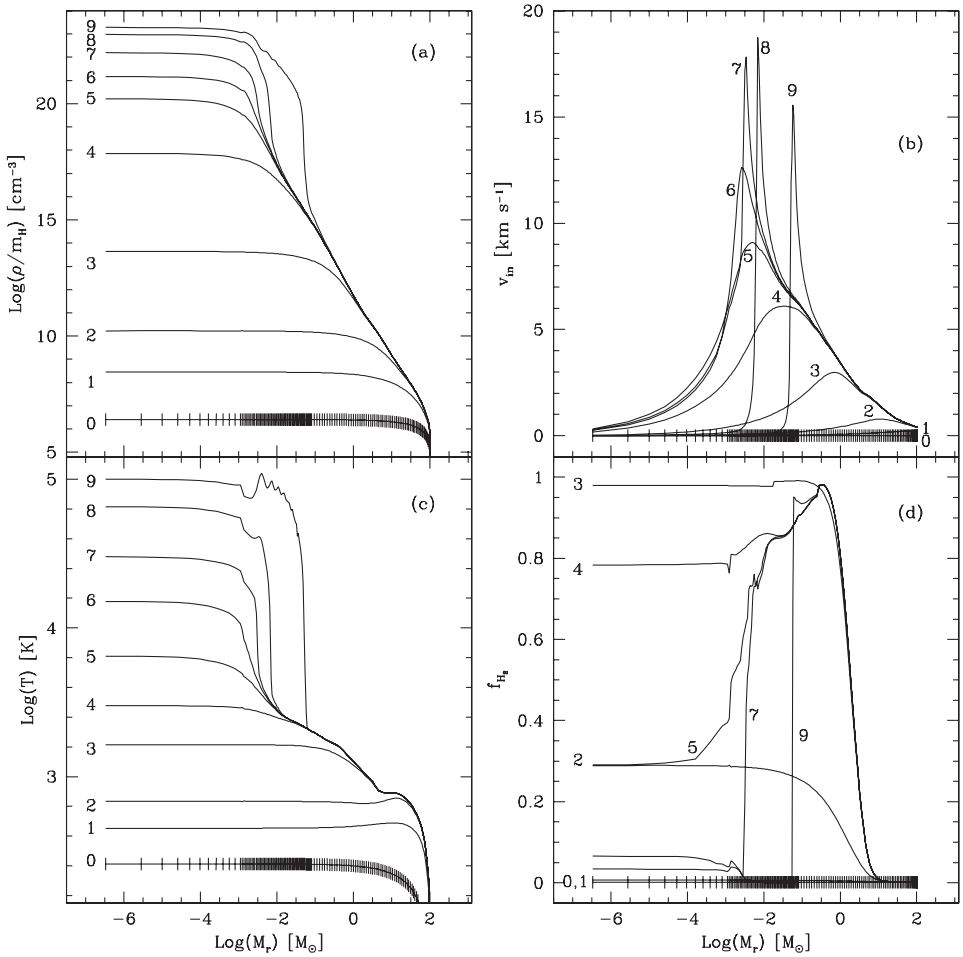

Figure 1. Spatial structure of the cloud in run P100/2 at 10 different stages of collapse (see Table 2). Panels refer to (a) density, (b) infall velocity, (c) temperature and (d) to the fraction of H nuclei inside H_2 molecules. On the abscissa we use the mass enclosed within radius r (M_r). Shell edges are denoted by small tags on to the curve referring to the initial configuration; in panel (d) we omit stages 6 and 8 for clarity. The small oscillations in the temperature profile of stage 9 around $M_r \simeq -2$ are a result of numerical effects.

Table 2. Collapse stages (run P100).

Stage	T_c (K)	Δt (yr)	$(t_f - t_i)$ (yr)	Notes
0	270	–	740 000	Initial conditions
1	450	720 000	20 000	Start rad. trans.
2	650	19 000	930	
3	1500	920	9.6	
4	3000	9.2	0.40	H_2 is dissociating
5	6500	0.060	0.34	
6	15 000	0.005	0.34	Core is forming
7	30 000	0.002	0.34	Core has formed
8	65 000	0.011	0.33	
9	100 000	0.33	–	Final stage

3.2.2 *Core formation*

During the last stages of the self-similar collapse (stages 5 and 6; evolution from point A to point B in Fig. 2), when the centre of the cloud is essentially adiabatic, H_2 dissociation acts as a 'thermostate', preventing a faster increase in temperature and pressure, which would halt the collapse. In fact, dissociation absorbs $\gtrsim$50 per cent of the heat generated by gas compression, which (owing to the opaqueness of the centre of the cloud) could not have been dissipated otherwise. When nearly all H_2 molecules are dissociated, the thermostatic effect is no longer effective, and the central temperature and pressure rise rapidly, stopping the collapse of the central regions. At the end of H_2 dissociation ($T_c \sim 20\,000$ K) the chemical energy and the thermal energy per H^0 atom are similar ($\simeq$2.2 and 2.6 eV, respectively). This fact reflects the virial theorem: half of the cloud gravitational energy is converted into thermal energy after compression, while the rest is tapped as chemical energy through dissociation.

Outside the core, the gas is still collapsing with a velocity close to that of free-fall. This results in a shock front forming at the edge of the core, where the infalling material is suddenly halted (see Fig. 1b). Unfortunately, the numerical method (i.e. the introduction of an artificial viscosity) used for the treatment of hydrodynamical effects is inaccurate when dealing with strong shocks, since they are spread over several shells. However, though the treatment of the shock physics is only approximate, the general picture of the cloud evolution is essentially correct. In run P100/2 we also improve the situation by refining the shells in the region where the shock forms.

The core evolution is driven by two main processes. First, as can be seen in Fig. 1(b), the core mass (defined as the mass inside the radius where the infall velocity is $< 0.1 v_{\rm ff}$, $v_{\rm ff} \equiv \sqrt{2GM_r/r}$) grows, owing to the accretion of infalling material. Secondly, even if the

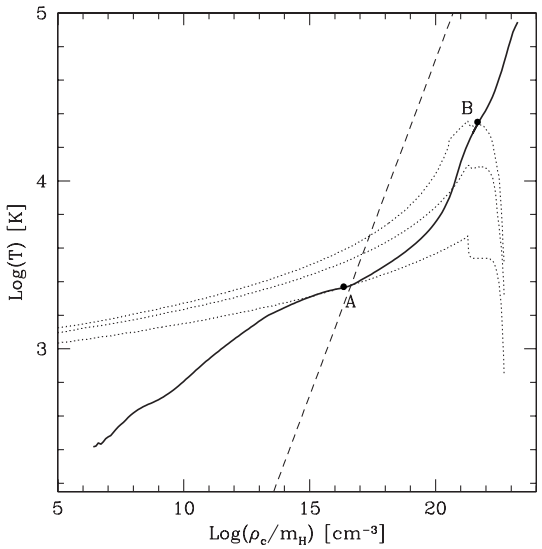

Figure 2. Evolution of the density and the temperature of the innermost shell (thick line). Points A and B mark conditions when the cloud becomes optically thick and when the hydrostatic core forms, respectively. Thin dotted lines show the loci of points where the equilibrium H_2 fraction is 0.9 (bottom), 0.1 (middle) and 0.01 (top). The dashed line show the theoretical locus of points where a generic cloud should become optically thick.

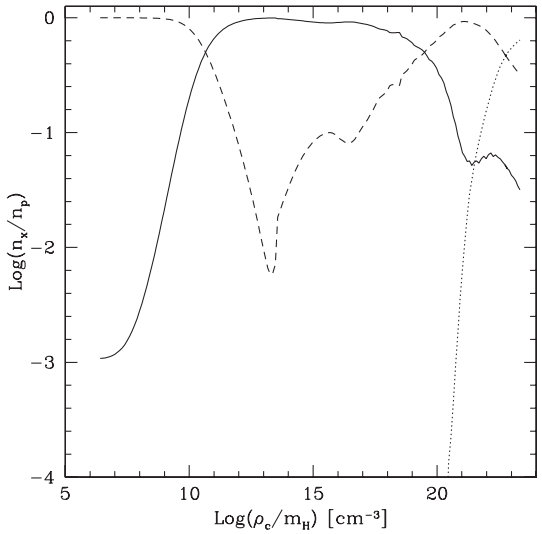

Figure 3. Evolution of the fractions of the main hydrogen species in the innermost shell as a function of density: H_2 (solid line), H^0 (dashed line) and H^+ (dotted line).

infall velocity is drastically reduced, the core is compressed by the infalling material, and then heats up (as can be seen in Fig. 2, beyond point B).

3.2.3 Cloud structure after core formation

After core formation and during its subsequent evolution, the H_2 fraction in the centre never rises again to important levels.[1] H_2 tends to form a layer of several solar masses between the small core

[1] The central value of f_{H_2} at late stages is quite uncertain: using the results of SCVH95 we obtain $f_{H_2} \sim 0.03$; had we used results such as those of Mihalas et al. (1988), we would have obtained $f_{H_2} < 0.01$; ON98 find $f_{H_2} \sim 0.4$, but this is likely to be too high since they do not consider pressure ionization effects.

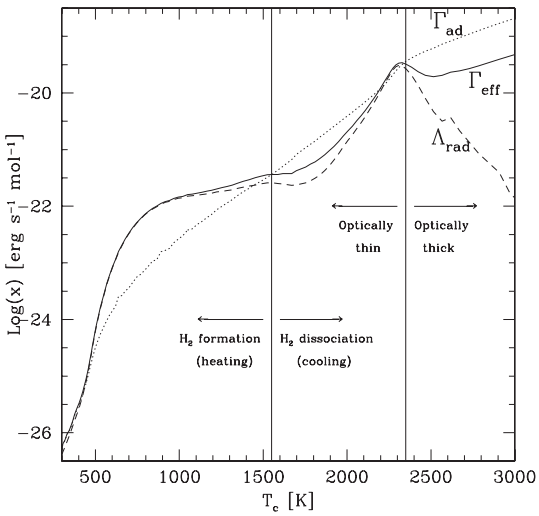

Figure 4. Radiative cooling rate (dashed), adiabatic heating rate (dotted) and effective (i.e. adiabatic plus chemical) heating rate (solid) in the innermost shell as a function of its temperature. The left vertical line marks the transition from H_2 formation to H_2 dissociation, while the right vertical line separates the optically thin and optically thick regimes.

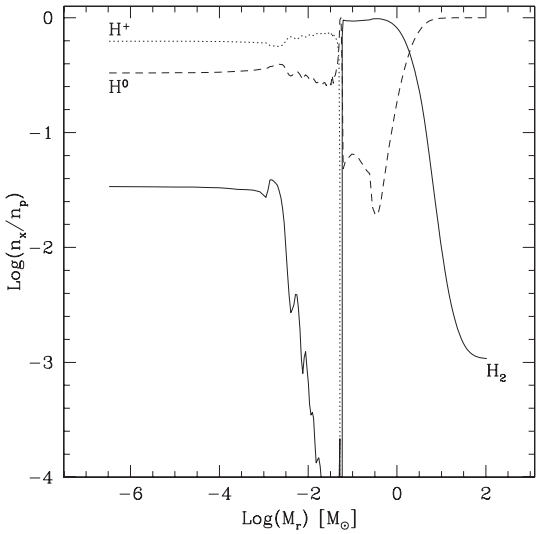

Figure 5. Chemical structure of the cloud at stage 9: H_2 (solid line), H^0 (dashed line) and H^+ (dot-dashed line); the ionized hydrostatic core, the inner molecular and the outer atomic envelope are quite apparent; the peak of the H^0 curve at $\log M_r \sim -1.3$ is located in the region where the (smoothed) shock brings down the infall velocity of the shell from the maximum value of ~ 15 to $\sim 2\,\mathrm{km\,s^{-1}}$. The small oscillations for $-2.5 \lesssim \log M_r \lesssim -1.5$ are numerical.

(where H is progressively ionized) and the outer layers (where H is essentially atomic, see Fig. 5). After stage 6 we can recognize three different regions, i.e. the core, the molecular envelope and the outer region (see Fig. 5).

(i) In the central core the infall velocity is much smaller than the free-fall value. At core formation, the gas here is basically neutral, but at stage 9 it has become mostly ionized (but n_{H^+}/n_H is still only ~ 2) because of the pressure ionization process. The outer edge of the core is marked by a shock front, where material accretes nearly with free-fall velocity. Since the artificial viscosity technique 'smooths' the shock, we have a thin transition region, where

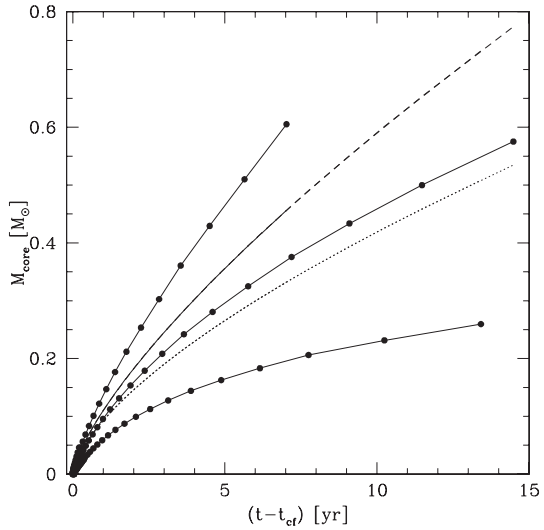

Figure 6. Evolution of the core mass. The three lines with dots refer to model P1000 (top line), P100 (middle line) and P10 (bottom line). The dashed line shows the predictions of ON98 (equation 11), while the dotted one shows the results of the calculation described in the text, using the parameters of run P100.

neutral H is the dominant species; but this may be a numerical artefact.

(ii) Outside the shock defining the core outer edge, there is an envelope of $\sim 3\,\mathrm{M}_\odot$ composed of molecular hydrogen (the shock also marks a sharp transition in chemical composition, from H_2 to H^0 or H^+). Such an envelope is essentially in free-fall ($v/v_{\rm ff}$ is in the range 0.3–0.7, decreasing outward). Its outer edge is roughly at a radius $\gtrsim 10^{15}$ cm.

(iii) The remaining outer gas, accounting for most of the cloud mass, has a chemical composition only slightly different from the initial one, since reactions leading to H_2 formation are slow (mainly because of the low density), and involve only a minor fraction of H atoms. This layer is the extension to the inner molecular envelope, and has a velocity $v/v_{\rm ff}$ of between 0.1 and 0.3.

At stage 9 the core temperature and density are $\simeq 10^5$ K and $\simeq 0.3\,\mathrm{g\,cm^{-3}}$, respectively. Under these conditions the Courant time-scale is extremely short ($\lesssim 300$ s.), and it becomes more and more difficult (and costly, in terms of CPU time) to follow the evolution further. For this reason, we stopped our calculations when the central temperature reached $\sim 10^5$ K.

3.2.4 *The accretion phase*

After core formation, the evolution continues because of the accretion of the outer envelope on to the core.

Despite our approximate treatment of the shock, we find that the accretion rate, as inferred from the full calculation, is extremely high: the core grows from $\sim 0.3 \times 10^{-2}\,\mathrm{M}_\odot$ when it forms, to $\sim 4.5 \times 10^{-2}\,\mathrm{M}_\odot$ in ~ 0.30 yr, which means $\dot{M} \sim 0.14\,\mathrm{M}_\odot\,\mathrm{yr}^{-1}$. Such accretion rate is much larger than typical estimates for present-day star formation ($\dot{M} \lesssim 10^{-4}\,\mathrm{M}_\odot\,\mathrm{yr}^{-1}$).

In order to extend our results to a more advanced state of accretion, we modified our code, 'freezing' the evolution of the shells deeply embedded in the core. In practice, when a shell has: (i) a small infall velocity ($v/v_{\rm ff} < 10^{-3}$), (ii) a high temperature ($> 5 \times 10^4$ K) and (iii) is located at least five shells inside the shell where the infall velocity is maximum, we completely stop its evolution (i.e. we set the velocity to zero and keep all the other quantities constant to the last computed values).

This greatly speeds up our calculations because there is no need to follow the shells with the shortest time-scales, drastically reducing the number of integration steps needed. Such 'freezing' is appropriate, since these shells do evolve on time-scales that are much longer than those imposed by the Courant condition and have little influence upon the layers where accretion occurs. There are two major concerns.

(i) The neglect of the secular changes in the core radius: for example, in the full calculation the radius of the 10 innermost shells undergoes a reduction of about 40 per cent (from 1.6 to 1.0×10^{10} cm) as $T_{\rm c}$ goes from 50 000 K (stage 8) to $\simeq 10^5$ K (stage 9), while in the simplified calculation performed between stages 8 and 9, we keep this radius constant. This change is less important in more external shells: the difference in the shock position between the 'full' and the 'frozen' run at stage 9 is found to be $\simeq 4$ per cent.

(ii) The radiation produced upon the shock surface could ionize a thin shell outside the shock itself, as reported in Staher, Palla & Salpeter (1986, hereafter SPS86), modifying the dynamics of accretion (see the next sections).

Instead, the influence of the lowered temperatures in the central shells is completely negligible, since the optical depth from the 'frozen' shells is very high ($\tau_{\rm c} \gtrsim 10^{12}$).

Fig. 6 shows the result of the accretion calculations performed with the modified code: we stop $\gtrsim 10$ yr after core formation. In the first 0.34 yr the results are almost identical to those obtained with the 'complete' code; points at later times should be considered as indicative only.

ON98 investigated the evolution of the mass accretion rate on the newly formed hydrostatic core using the Larson–Penston self-similar solution (L69; Penston 1969) and its extensions after core formation (Hunter 1977; Yahil 1983; Suto & Silk 1988). For a model close to our model P100 (and P100/2), they found that the core mass grows following a power law

$$M_*(t) = 0.11\,\mathrm{M}_\odot[(\mathrm{t} - \mathrm{t_{cf}})/\mathrm{yr}]^{0.73}. \quad (4)$$

We also find an empirical model that could better fit the numerical results, based on the fact that in our calculations we find that the mass flux $M_{\rm flux}(M_r) = 4\pi r^2 \rho v_{\rm in}$ is well approximated by a power law. Such an empirical model leads us to predict that

$$M_*(t) = 9.2 \times 10^{-2}\,\mathrm{M}_\odot \left(\frac{\mathrm{t}}{\mathrm{yr}} + 0.0063\right)^{0.657}. \quad (5)$$

Both of these analytical expressions are compared with the numerical results in Fig. 6.

3.2.5 *Importance of initial conditions*

The above description essentially applies to all the models we computed: the evolutionary sequence is always the same, even if there are small quantitative differences. Models lose memory of the initial conditions almost completely during the self-similar phase, as can be seen in Fig. 7, where tracks referring to the different models are very close for $n_{\rm c} > 10^{14}\,\mathrm{cm^{-3}}$, i.e. well before the cloud becomes optically thick (point A) or forms the central hydrostatic core (point B).

There remain only relatively small differences (within a factor of 2 or 3), in particular:

(i) models with higher total mass ($M_{\rm tot}$), have higher temperatures than low-$M_{\rm tot}$ models, for any given central density $n_{\rm c}$;
(ii) models with high $M_{\rm tot}$ have cores that grow faster than low-$M_{\rm tot}$ models (see Fig. 6).

Both of these trends can be easily explained: when we impose that in the initial stage the clouds are close to equilibrium, we implicitly force high-mass models to have higher temperatures at any given density; even if quantitative differences are strongly reduced in the self-similar phase, high-mass models remain warmer than low-mass models at all stages. Furthermore, the accretion rate depends on temperature, since $\dot{M} \sim M_{\rm Jeans}(T,\rho)/t_{\rm ff}(\rho) \propto T^{3/2}$ (see Stahler, Shu & Taam 1980a,b) and the temperature differences also explain those in $\dot{M}$.

The behaviour of the N1500 model (the only one for which we do not impose quasi-equilibrium initial conditions) is particularly relevant: after some 'wandering' in the $n_{\rm c}$–$T_{\rm c}$ plane, its central conditions evolve almost exactly along the evolutionary track of model P100, indicating that the collapse does not preserve the memory of initial conditions and the cloud evolves along an equilibrium track.

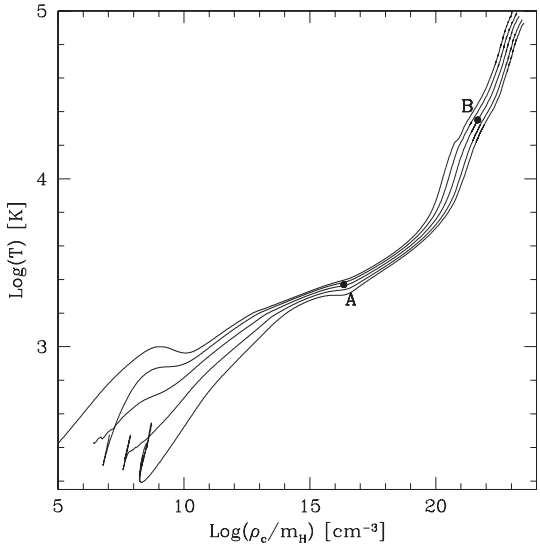

Figure 7. Comparison of the evolution of central conditions (density and temperature) in several of our computed models: from top to bottom, the lines refer to model P1000, I1000, P100, I100 and P10; model N1500 is almost indistinguishable from model P100, except in the first stages. As in Fig. 6, points A and B denote the conditions where (in model P100) τ first becomes >1 and where core formation occurs, respectively.

3.3 The radiation field

The evolution of the radiation field is intimately coupled with dynamics, and our physical description of forming primordial stars fully accounts for their emission properties. Here we give details of the evolution of the optical depth, luminosity and spectra during the two phases of collapse and core formation, and at the very beginning of the accretion phase.

3.3.1 Luminosity from the collapsing cloud

At the onset of dynamical evolution, radiation results from the cooling of the optically thin H_2 present in the cloud. At stage 1, as three-body reactions keep converting H atoms into H_2 molecules, the optical line depth grows rapidly, reaching significant values. At stage 2 there are already 14 lines with $\tau > 0.1$ (although none of them with $\tau = 1$), and this number rises to 42 lines (half with $\tau > 1$) by the time the central temperature reaches 1000 K (between stages 2 and 3). In Fig. 8(a) we show, as an illustrative example, the evolution of the optical depth profile for a selected line during the self-similar phase.

The increase of the optical depth obviously affects the gas cooling properties (as can be seen from the flattening of the radiative cooling curve in Fig. 4), but it does not influence the dynamics in a fundamental way. The increase in H_2 abundance is associated with an increase of the gas temperature and of the number of relevant transitions of the H_2 molecule. As the temperature grows, new, high quantum number lines are initially optically thin, providing a minimum level of cooling. Though line

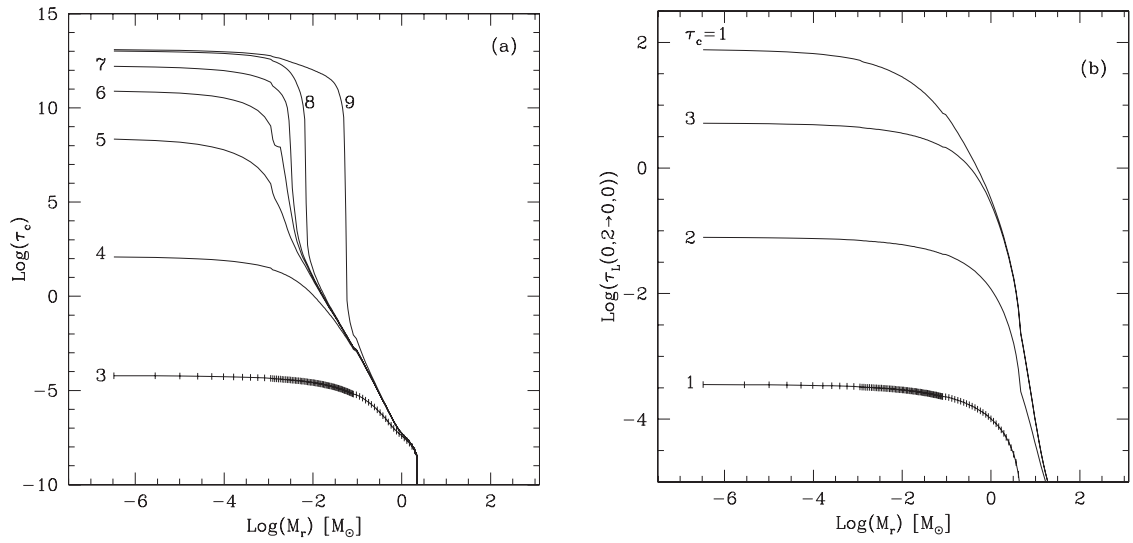

Figure 8. The radial outward optical depth as a function of enclosed mass for (a) continuum radiation and (b) for radiation at the centre of the roto-vibrational H_2 $(0,2) \rightarrow (0,0)$ transition ($\lambda = 28.3\,\mu$m); the top curve in this panel, taken when $\tau_{\rm c} = 1$, is represents all stages between 4 and 9.

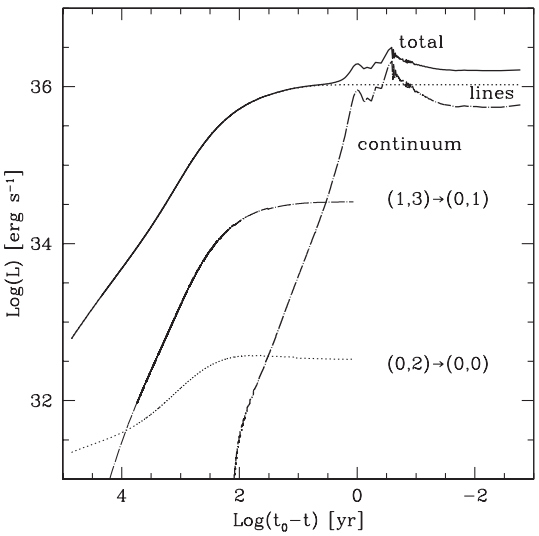

Figure 9. Evolution of the luminosity in lines (heavy dotted), continuum (heavy dot-dashed) and their sum (thick solid line); thin lines refer to two H_2 transitions: $(0,2) \rightarrow (0,0)$, $\lambda = 28.3\,\mu$m (dotted) and $(1,3) \rightarrow (0,1)$, $\lambda = 2.12\,\mu$m (dot-dashed); they do not appear when we 'freeze' all line luminosities. Note that the x-axis shows the time left before the end of our calculation. The oscillations in the continuum luminosity between $0.5 \gtrsim \log(t_0 - t) \gtrsim -1$ are connected with core formation and could be partially numerical.

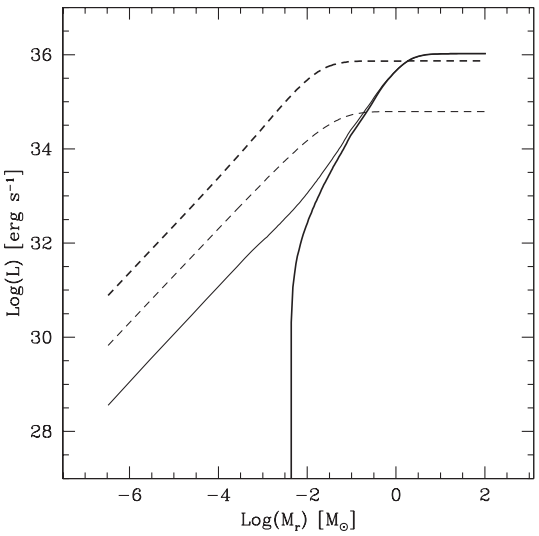

Figure 10. Outward total luminosity in H_2 lines (solid) and in the continuum (dashed) as a function of enclosed mass at two different times: when $T_c = 2000\,$K, $\tau_c \lesssim 0.1$ (thin lines) and when $T_c \sim 2300\,$K, $\tau_c \sim 10$ (thick lines).

cooling is severely quenched by opacity (e.g. at $T_c \simeq 2000\,$K only a fraction $\simeq 0.02$ of the line flux is not re-absorbed locally) its absolute value *increases* as T_c increases; this prevents the temperature from rising too fast, possibly stopping the collapse in its early phases.

As already mentioned, when $T_c = 1000\,$K we start to include cooling from the continuum, which rapidly gains importance, becoming the dominant process in the central $\sim 0.1\,M_\odot$ when $T_c \sim 1800\,$K. The evolution of the continuum opacity profile is shown in Fig. 8(b), where the formation of the core sharp edge is apparent.

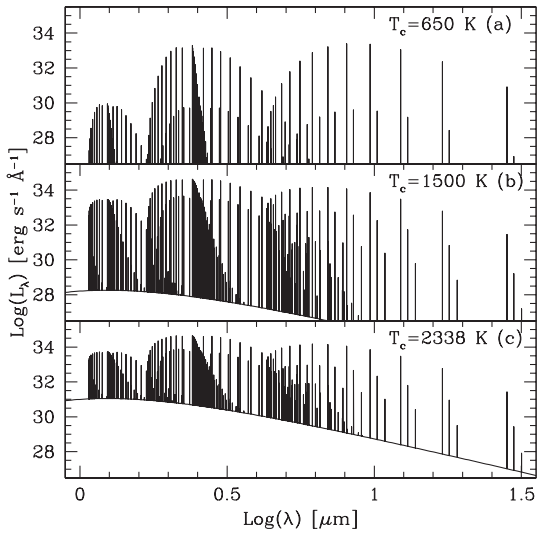

Figure 11. Emitted spectra when T_c is (a) 650 K, (b) 1500 K and (c) 2338 K (i.e. just before we 'freeze' lines). Linewidths are actually smaller ($\Delta\lambda/\lambda \lesssim 10^{-4}$) than the line thickness in this plot, so that overlaps are only apparent.

The corresponding emitted luminosities versus time are plotted in Fig. 9. Note that even when continuum radiation dominates the central emission, the H_2 lines still have a comparable or slightly larger overall luminosity. This is a result of the fact that line radiation comes from the outer, massive H_2 envelope, while the continuum comes from an inner, much smaller region (only slightly larger than the core itself). This can be seen in Fig. 10, where we show the radial dependence of the emitted luminosity; in particular, note that the drop in the central line luminosity has a negligible influence upon the total line luminosity, and that the growth of continuum luminosity stops at $M_r \sim 10^{-2}$–$10^{-1}\,M_\odot$, while the line luminosity is still growing at $M_r \sim 1\,M_\odot$.

3.3.2 Spectra

In Fig. 11, we show the emitted spectra at three different stages. In the upper panel the spectrum comes from line emission only, while in the lower panels we assumed that the continuum spectrum is a blackbody at the effective temperature of the central shell (1500 K, panel b) and of the continuum photosphere (i.e. of the region where the radial outward optical depth is ~ 1). Such a temperature remains roughly constant at $\simeq 2300$–$2400\,$K from the birth of the continuum photosphere to the end of our calculations.

In appendix B we give a full listing of the luminosities of all the calculated lines, plus the integrated continuum luminosity at four stages (the three depicted in Fig. 11 plus the stage when $T_c = 1000\,$K). We note that the durations of the various stages are very different: line luminosities resemble those listed in the L_{650} column (corresponding to Fig. 11a) for $\sim 10^4\,$yr, while they resemble those given in columns L_{1000}, L_{1500} and $L_{\tau_c=1}$ only for ~ 300, 40 and 2 yr, respectively.[2]

We note that the spectra are produced only in the central collapsed region: line emission comes essentially from the

[2] The last duration ($\sim 2\,$yr) is actually only a lower limit, since line emission is still at high levels when our calculations stop; however, the H_2 envelope where line emission originates is not likely to last for $\gtrsim 100\,$yr after core formation, since it could be accreted on to the core, or photodissociated because of the outgoing radiation.

molecular envelope, while continuum emission is produced close to the surface of the hydrostatic core. In practice, the whole of the protostellar luminosity comes from the central $\sim 3\,M_\odot$. The structure of this central region is quite similar in all the models, since it is largely determined by the self-similar collapse, rather than by initial conditions. For this reason, the spectra emitted by different clouds during these phases should be similar.

3.3.3 Radiation pressure effects

We have found that the role of radiative force is negligible during all the stages of evolution we followed, i.e. at least until the first phases of accretion (our stage 9). In a test run we removed the radiative term in the momentum equation and re-calculated evolution. We then compared the results with those of the 'full' code, and found that the difference was completely negligible.

Returning to the early phase of accretion, despite the very high luminosity ($\sim 10^{36}$ erg in the continuum plus another $\sim 10^{36}$ erg in H_2 lines), which is comparable with the Eddington luminosity, $L_{\rm Edd} \simeq 1.25 \times 10^{36} [M/(0.01\,M_\odot)]$ erg, the opacity of the infalling gas is much smaller than the electron scattering opacity ($\kappa_{\rm es} = \sigma_{\rm T}/m_{\rm H} \simeq 0.4\,{\rm cm^2\,g^{-1}}$), since the infalling material is essentially molecular, with a very low ionized fraction, and other opacity sources (Rayleigh scattering, bound–free and free–free transitions, collision-induced absorption of H_2) give small contributions. We find that the opacity is everywhere less than $0.05\kappa_{\rm es}$ at all times before the formation of the hydrostatic core; typical values are actually several order of magnitude less than these upper limits. The same is also true after the formation of the hydrostatic core, if we consider only the accreting layers.

3.3.4 Bridging collapse models with accretion models

SPS86 and recently Omukai & Palla (2001) studied the subsequent phase of accretion by modelling the hydrostatic core as a star of increasing mass, surrounded by an infalling envelope, the structure of which was determined by an assumed steady mass accretion rate $\dot{M}_* = 4.4 \times 10^{-3}\,M_\odot\,{\rm yr^{-1}}$. They found that the shock surface is inside an optically thick ionized region, the outer edge of which is roughly coincident with the photosphere. They also found that between the shock front and the photosphere the radiative force term is important, since $\kappa \simeq \kappa_{\rm es}$ and the luminosity is not far from the Eddington value. Despite this fact, both works find that the radiative force is not able to stop the accretion before the core mass grows to very high values ($> 100\,M_\odot$).

We find that also in our models the shock front is inside the optically thick region, but the gas between the shock and the photosphere is not ionized, mainly because the density in the region is relatively high ($\sim 10^{-6}\,{\rm g\,cm^{-3}}$), about 1000 times larger than the value that can be estimated from fig. 12 of SPS86; instead, we find that the temperature is only slightly lower than in the model of SPS86. The ionization fraction inside such a region is low and remains so ($\lesssim 0.05$) even if we make the hypothesis that radiation coming from the shock heats the gas inside the photospheric shells, so that the gas and the radiation temperature are the same ($\simeq 12\,000$ K, the post-shock temperature found both by our calculations and those of SPS86). So, this gas still has a low opacity, and the radiative force is small.

Although numerical effects could play some role in this discrepancy, the most likely explanation is that the models of SPS86 are admittedly indicative for core masses $\lesssim 0.1\,M_\odot$, i.e. during the 'decay of transients' phase, when the arbitrarily chosen initial conditions are still important; instead in our models the core mass is always in this range (here we do not consider the simplified calculations aimed at studying the growth of the core mass). It is quite possible that both results are correct and that a transition occurs after the last stage of our calculations. For instance, we note that the difference in the density of the photospheric layers (which keeps the ionization fraction at low levels) is mainly the result of the large difference (a factor of ~ 100) between the accretion rate we find and that assumed by SPS86; since in our models we also find that the mass accretion rate is decreasing, such a difference will reduce.

3.4 Comparison with metal-rich protostars

In this section we discuss the similarities and differences between the PopIII (high-redshift, zero-metal) star formation process we addressed and the PopI–PopII (low-redshift, solar metallicity) star formation.

3.4.1 Hydrostatic core

In our work (and also in that of ON98) the birth of the quasi-hydrostatic core is quite different to that described by L69 [and more recently by Masunaga, Miyama & Inutsuka (1998) and Masunaga & Inutsuka (2000)] for a present-day protostar because of the very different conditions. In fact, those authors found that a molecular core forms first, and only later on does H_2 dissociation lead to the formation of a second more internal core, which is now ionized and at much higher temperature and density, as can be seen in Table 3. The two cores coexist for a short time, while the second core 'absorbs' the first one.

Instead, in our models we find a single core, completely different from the first (molecular) core of metal-rich models, but closely resembling the latter.

The reason for both the differences and the similarities between the two cases is explained essentially by an argument from Omukai (2000). He found that the locus of points in the n–T plane where $\tau \sim 1$, $M \sim M_{\rm Jeans}(T, n)$ and $\Lambda_{\rm rad} \sim \Gamma_{\rm ad}$ (cfr. Silk 1977) is approximately described by a line (L) with $T \propto n^{2/5}$, which is shown in Fig. 2; on the right of L, a core with mass $\geq M_{\rm Jeans}(T, n)$ is optically thick.

Our metal-free models become optically thick at point A (remarkably close to L), where $T_{\rm c}$ is high and H_2 dissociation is immediately effective, preventing the formation of a hydrostatic core. Instead, metallic protostars ($Z \gtrsim 10^{-6}\,Z_\odot$) reach L at temperatures that are too low for H_2 dissociation, and the first (molecular) core forms. Such a core evolves adiabatically, i.e. along a $T \propto n^{\gamma_{\rm ad}-1}$ line, which remains close to L, because $\gamma_{\rm ad} \sim \gamma_{\rm ad,H_2} \simeq 7/5$. In this way cores of all metallicities converge towards the vicinity of point

Table 3. Comparison of quasi-hydrostatic cores initial properties.

	P100	L69(I)	L69(II)
$M/(10^{30}\,{\rm g})$	6	10	3
$R/(10^{11}\,{\rm cm})$	1	600	9
$T_{\rm c}/{\rm K}$	2×10^4	200	2×10^4
$\rho_{\rm c}/({\rm g\,cm^{-3}})$	1×10^{-2}	2×10^{-10}	2×10^{-2}
f_{H_2}	$\lesssim 0.03$	$\simeq 1$	$\simeq 0$

P100: results of our run P100; L69(I): first core of Larson (1969); L69(II): second core of Larson (1969).

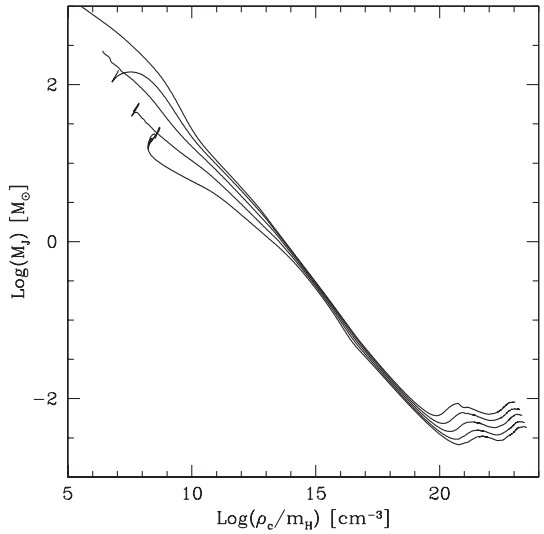

Figure 12. Evolution of the central Jeans mass (i.e. the Jeans mass calculated assuming $\rho = \rho_c$, $T = T_c$) for several computed models (from top to bottom: P1000, I1000, P100, I100 and P10). Models P100/2 and N1500 are not shown but they are almost indistinguishable from model P100.

A. After point A, the evolution of the central regions is essentially determined by the balance between compressional heating and H_2 dissociation cooling and no longer depends on the metal content. Thus, metal-rich and metal-free models form a core when H_2 is exhausted, close to point B.

The initial core mass $\sim 3 \times 10^{-3}\,M_\odot$ (only slightly dependent upon initial conditions) agrees with $M_{\rm Jeans}(T_{\rm B}, n_{\rm B})$ (where the subscript B denotes the values at point B). Such a mass is also close to the minimum value reached by $M_{\rm Jeans}(T_c, n_c)$ during the evolution of the cloud (see Fig. 12). This minimum Jeans mass is generally interpreted as the minimum fragment mass (i.e. the mass below which further fragmentation is impossible) and we find that it depends very weakly upon initial conditions and on metallicity. An important corollary is that the minimum fragment mass cannot be simply found by imposing $\tau \gtrsim 1$, since we have seen that such a condition, although necessary, is not sufficient for the formation of a stable hydrostatic core.

It is also interesting to note that in our models there is no sign of instability inside the hydrostatic core owing, for example, to H ionization, even if the core is mostly atomic at stage 7 and mostly ionized at stage 9.

3.4.2 *Accretion rate*

Even if important core properties, such as the initial mass and the evolutionary path of central regions in the n–T plane are almost independent of metal content, the mass accretion rates are completely different, with metal-free objects accreting at a rate $\gtrsim 10^3$ times larger than their metal-enriched counterparts. For example, in our P100 model the core mass reaches $\sim 0.3\,M_\odot$ in ~ 6 yr (see Fig. 6), while in the model of Masunaga & Inutsuka (2000) about 20 000 yr are required for the accretion of the same mass (see their fig. 7).

As already discussed by several authors (e.g. Stahler et al. 1980a,b; SPS86), the reason for this difference is found in the initial conditions; in particular, in the higher temperature, since for an object with $M \sim M_{\rm Jeans}$ we have

$$\dot{M} \sim (k/m_{\rm H})^{3/2} T^{3/2}/G \sim 1.8 \times 10^{-7} T^{3/2}\,M_\odot\,{\rm yr}^{-1}. \quad (6)$$

If we take a typical initial temperature for our model, ~ 300 K, we obtain $\dot{M} \sim 10^{-3}\,M_\odot\,{\rm yr}^{-1}$, but if we take $T \sim 5$ K, as would be appropriate for present-day protostellar clouds, we obtain a value ~ 500 times smaller for $\dot{M}$.

We note that (6) gives the *mean* accretion rate for the *complete* accretion of the protostellar cloud on to the core; if we consider accretion of only a fraction of the cloud, equation (6) would give higher values of $\dot{M}$ because the appropriate reference temperature would be higher.

3.4.3 *Radiation feedback*

In the previous sections we showed that radiation pressure is not effective in stopping the accretion flow upon a zero-metallicity protostellar core. The case of metal-rich protostars is different: luminosities are smaller because of smaller accretion rates, but the presence of dust brings the opacity to much higher levels. For example, Stahler, Shu & Taam (1981) estimate that at the start of accretion radiative deceleration retards the inflow to 42 per cent of the free-fall value, even if it cannot completely stop accretion [see also the models of Masunaga et al. (1998) and Masunaga & Inutsuka (2000), which include radiation pressure effects in their momentum equation]. In a different context, radiative forces upon dust were also found to act decisively in halting the accretion inflow upon massive stars (Wolfire & Cassinelli 1987; Larson & Starrfield 1971).

For sufficiently high density and temperature, ignition of nuclear reactions occurs in the core interior. To check whether the effect can, in principle, stop the accretion phase, we compare the accretion time-scale with the diffusion time-scale of the energy produced.

As can be seen in Fig. 8, the interior of the core has an optical depth $\tau_* \gtrsim 10^{12}$. If energy is transported radiatively, the time-scale for its diffusion through the core is $t_{\rm diff} \simeq \tau_* R_*/c \simeq 10^5\,{\rm yr}[\tau_*/10^{12}][R_*/(10^{11}\,{\rm cm})]$, where the core radius R_* has a value of the order of 5×10^{11} cm. We note that as T_c rises, the opacity κ inside the core decreases; anyway, $\kappa \gtrsim \kappa_{\rm es}$, which leads to a strong lower limit, $\tau_* \gtrsim 10^{10}$.

An identical calculation for present-day protostellar cores leads to a time-scale of the same order of magnitude. Instead, the accretion times differ enormously. For example, if we extrapolate equation (5), we find that our core would take only $t_{1\odot} \sim 40$ yr after formation to reach a mass of $M_* \simeq 1\,M_\odot$ (but we note that $t_{1\odot} \sim 250$ yr in the models of SPS86), while in the model by Masunaga & Inutsuka (2000) more than $t_{1\odot} \sim 1.4 \times 10^5$ yr are required for the core to reach the same mass.

So, $t_{1\odot}/t_{\rm diff} \sim 1$ in metal-rich cores, but $t_{1\odot}/t_{\rm diff} \ll 1$ in the metal-free case. Accordingly, in the metal-free case the energy generated in the core centre (for instance, because of the ignition of nuclear reactions) cannot affect the accretion, while in the metal-rich case such energy could be capable of reaching the surface and changing the conditions of the infalling envelope.

The arguments discussed in the present section are subject to important uncertainties. For example, we did not investigate any energy transport mechanisms, such as convection, different from radiative diffusion, which could be much more efficient (e.g. see the 'luminosity wave' described in SPS86).

4 LINE FLUX AND DETECTABILITY

The work by KS02 has addressed the important problem of detectability of the emission from collapsing primordial protostar.

They employed approximate analytical calculations (partially derived from the ON98 work) in order to estimate order-of-magnitude luminosities of collapsing objects, assuming a central temperature $T \sim 1000$ K.

In Table 4 we list the luminosities of five important lines, at all the four stages we tabulated in Table B1, plus the total line luminosity, the continuum luminosity and their sum. They are compared with the values predicted by KS02.

It can be seen that KS02 predicts a total luminosity comparable with our results for the initial phases of collapse; instead, in the last phases our total luminosities are $\gtrsim 10$ times larger than the KS02 value. This is quite reasonable, since the approximations they used are much better at the beginning of the collapse than at the end. If we consider the luminosities of single lines, a more important discrepancy emerges. KS02 correctly predict that the rotational transition at $\lambda = 9.69\,\mu$m is the most important one at the beginning, but they estimate a very high line luminosity, which no lines actually achieve, even in advanced stages. The reason is that they attribute too large a fraction of the total luminosity to single lines. Instead, the emission is actually split into a growing number of lines. In the early phases, the two rotational lines listed in Table 4 account for ~ 50 per cent of the total emission (first tabulated stage), but the luminosities of single lines 'saturate' when their central optical depth becomes $\gtrsim 1$. As the total line emission rises, we have mainly an increase in the number of important lines, rather than a growth of the luminosity of single lines: at the last stage no line accounts for more than ~ 5 per cent of the total line emission.

In Table 4 we also give the expected specific fluxes coming from a single protostellar object at a redshift of $z = 19$ in an SCDM cosmological model for the first and the last listed stage. It can be seen that the most promising lines are those produced by purely rotational transitions, such as those at $\lambda = 9.69$ and $8.06\,\mu$m (which are redshifted to $\lambda_{\rm obs} \simeq 190$ and $160\,\mu$m, respectively), whose expected specific flux is $\gtrsim 10$ nJy for at least $\sim 10^4$ yr); vibrational transitions, such as those at $\lambda = 2.41$ and $2.81\,\mu$m (redshifted to $\lambda_{\rm obs} \simeq 48$ and $56\,\mu$m) reach specific fluxes of the same order only in the last phases and their emission at such levels should only last for $\lesssim 10^3$ yr. Finally, we predict that the continuum specific flux should be of the order of 0.002 nJy at an observed wavelength of $\lambda_{\rm obs} \sim 40\,\mu$m (from a rest-frame wavelength of $\sim 2\,\mu$m); we cannot predict the duration of continuum emission, since it is deeply affected by the evolution of the accretion and by the evolution of the hydrostatic core at the centre.

Such fluxes are largely below the detection threshold of any observational facility that will be available in the near future. NGST sensitivity for continuum radiation should be of the order of $\sim 1\,\mu$Jy at $\lambda = 20\,\mu$m, while ALMA should reach a sensitivity of ~ 10 mJy for a line 25 km s^{-1} wide at $\lambda \simeq 350\,\mu$m. However, the possibility that primordial protostars form in large groups must not to be excluded, since a galactic-scale (10^{11}-M$_\odot$) fluctuation could host a large number of 10^6-M$_\odot$ haloes, and each of them could host several protostellar objects. For instance, KS02 roughly estimate that a galactic-scale fluctuation could have a luminosity $\sim 10^4$ times larger than a single object, and that such a luminosity could last for $\sim 10^7$ yr. If this is correct, specific fluxes from galactic-scale objects should be of the order of $\sim 0.01\,\mu$Jy and ~ 0.1 mJy for continuum and line emission, respectively.

Table 4. Comparison of line and continuum luminosities; luminosities (L) are in units of 10^{34} erg s^{-1}, specific fluxes at earth (l, for an object at $z = 19$ in a SCDM cosmology with $H_0 = 75$ km s^{-1} Mpc^{-1}) in nJy; the continuum specific flux is calculated at the peak of the blackbody spectrum ($\lambda \simeq 2\,\mu$m). All data come from run P100/2

$\lambda(\mu$m)	L_{650}	L_{1000}	L_{1500}	$L_{\tau_c=1}$	L(KS02)	l_{650}	$l_{\tau_c=1}$
2.41	0.20	2.21	3.90	4.26	0.4	0.6	13
2.81	0.18	2.49	4.22	4.55	–	0.7	16
8.06	0.99	3.48	3.72	3.74	–	10	37
9.69	1.12	2.78	2.90	2.90	5.5	14	35
28.3	0.01	0.03	0.03	0.03	0.8	0.3	1.0
Line total	4.4	43	89	106	6.7	–	–
Continuum	–	0.00	0.13	75	–	–	0.002
Total	4.4	43.2	89.3	181	6.7	–	–

5 CONCLUSIONS

In this work we have investigated the evolution of the luminosity and spectra of the radiation emitted by primordial collapsing protostars. We find that initially radiation comes mostly from H_2 rotational lines. Later, the contributions from H_2 vibrational lines and also from continuum radiation (owing to the accretion upon a centrally hydrostatic core) become important. At early stages, only two rotational lines account for about 50 per cent of the total emission, but the subsequent increase in total line luminosity results in an increase of the number of prominent lines, rather than a large increase in the luminosity of the most important ones. As a result, the expected line-specific fluxes are always $\lesssim 50$ nJy (with linewidths $\lesssim 30$ km s^{-1}), even for the most important lines, which should fall at observed wavelengths in the range $150-200\,\mu$m. Continuum radiation should reach a specific flux of the order of 0.002 nJ, peaking at an observed wavelength between 20 and $40\,\mu$m. These fluxes should be quite universal, provided that a molecular central region of ~ 3 M$_\odot$ develops at the centre of each protostellar cloud. The predicted fluxes, both for line and continuum radiation, are largely below the detection threshold of existing or planned instruments (such as NGST and ALMA), but the possibility that primordial protostars form large 'clusters' remains to be investigated, even if rough estimates do not look very promising (KS02).

In our work we also found that, different from the present-day case, radiation forces play virtually no role in the initial evolution of a protostellar object (i.e. during the self-similar collapse, the formation of the core and the onset of accretion). Although we were not able to completely bridge the gap with accretion models such as those of SPS86 and Omukai & Palla (2001), we have shown that their initial assumptions are quite reasonable. Even if there are differences in the ionization structure, there is an indication (in particular, the decrease in the mass accretion rate) that these will vanish as the hydrostatic core mass grows. Thus, undisturbed spherical collapse should proceed until the initial protostellar cloud has been largely accreted, or until radiation forces halt the infall at $M_* \sim 300$ M$_\odot$ (Omukai & Palla 2001).

What can stop mass growth is the presence of HD molecules (even in a tiny fraction) that may result from shocks (Flower & Pineau des Forêts 2001; Uehara & Inutsuka 2000); in this case the fragmentation of the PopIII object might end up in clumps of roughly solar rather than thousand solar masses, thus drastically changing the final mass of the star.

If this process is not important and angular momentum and magnetic fields do not play a significant role either, the final mass of a primordial protostar is primarily set by the amount of gas available in the parent cloud. Then, it is conceivable that the primordial IMF is skewed towards high masses, and that very massive stars (VMS), with masses in excess of $M \sim 100$ M$_\odot$, can

form. Such stars may end-up as a population of intermediate mass black holes (Portinari, Chiosi & Bressan 1998; Heger & Langer 2000) that represent the end product of such an episode of pre-galactic star formation. Then, these seeds could be incorporated into the larger units as seen in the bulges of present-day galaxies (Madau & Rees 2001).

ACKNOWLEDGMENTS

We thank an anonymous referee for a critical reading and of the manuscript and for stimulating remarks. We also thank B. Ciardi for discussions and for making her chemistry routines available to us, and K. Omukai, R. Nishi and F. Palla for discussions and clarifying remarks concerning their works.

REFERENCES

Abel T., Anninos P., Norman M. L., Zhang Y., 1998, ApJ, 518
Abel T., Bryan G. L., Norman M. L., 2000, ApJ, 540, 39 (ABN00)
Bowers R. L., Wilson J. R., 1991, Numerical Modeling in Applied Physics and Astrophysics. Jones Bartlett, Boston, MA
Bromm V., Coppi P. S., Larson R. B., 1999, ApJ, 527, L5
Bromm V., Ferrara A., Coppi P. S., Larson R. B., 2001, MNRAS, 328, 969
Bromm V., Coppi P. S., Larson R. B., 2002, ApJ, 564, 23 (BCL02)
Ciardi B., Ferrara A., 2001, MNRAS, 324, 648
Flower D. R., 2000, MNRAS, 318, 875
Flower D. R., Pineau des Forêts G., 2001, MNRAS, 323, 672
Fontaine G., Graboske H. C., Jr, Van Horn H. M., 1977, ApJS, 35, 293
Fuller T. M., Couchman H. M. P., 2000, ApJ, 544, 6
Gnedin N. Y., Ferrara A., Zweibel E. G., 2000, ApJ, 539, 505
Haiman Z., Thoul A. A., Loeb A., 1996, ApJ, 464, 523
Heger A., Langer N., 2000, ApJ, 544, 516
Hummer D. G., Mihalas D., 1988, ApJ, 331, 794
Hummer D. G., Rybicki G. B., 1971, MNRAS, 152, 1
Hunter C., 1977, ApJ, 218, 834
Hutchins J. B., 1976, ApJ, 205, 103
Irwin A. W., 1981, ApJS, 45, 621
Kamaya H., Silk J., 2002, MNRAS, 332, 251 (KS02)
Kolb E. W., Turner M. S., 1990, The Early Universe. Addison-Wesley, Reading, MA
Larson R. B., 1969, MNRAS, 145, 271 (L69)
Larson R. B., Starrfield S., 1971, A&A, 13, 190
Lenzuni P., Chernoff D. F., Salpeter E. E., 1991, ApJS, 76, 759
Machacek M. E., Bryan G. L., Abel T., 2001, ApJ, 548, 509
Madau P., Rees M. J., 2001, ApJ, 551, 27
Masunaga H., Inutsuka S., 2000, ApJ, 531, 350
Masunaga H., Miyama S. M., Inutsuka S., 1998, ApJ, 495, 346
Mihalas D., Däppen W., Hummer D. G., 1988, ApJ, 331, 815 (MDH88)
Nakamura F., Umemura M., 1999, ApJ, 515, 239
Nakamura F., Umemura M., 2001, ApJ, 548, 19
Nishi R., Susa H., 1999, ApJ, 523, 103
Omukai K., 2000, ApJ, 534, 809
Omukai K., Palla F., 2001, ApJ, 546, 635
Omukai K., Nishi R., 1998, ApJ, 508, 141 (ON98)
Palla F., Salpeter E. E., Stahler S. W., 1983, ApJ, 271, 632
Penston M. V., 1969, MNRAS, 144, 425
Portinari L., Chiosi C., Bressan A., 1998, A&A, 334, 505
Rogers F. J., Iglesias C. A., 1992, ApJS, 79, 507
Saumon D., Chabrier G., van Horn H. M., 1995, ApJS, 99, 713
Sauval A. J., Tatum J. B., 1984, ApJS, 56, 193
Silk J., 1977, ApJ, 214, 152
Stahler S. W., Palla F., Salpeter E. E., 1986, ApJ, 302, 590 (SPS86)
Stahler S. W., Shu F. H., Taam R. E., 1980a, ApJ, 241, 637
Stahler S. W., Shu F. H., Taam R. E., 1980b, ApJ, 242, 226
Stahler S. W., Shu F. H., Taam R. E., 1981, ApJ, 248, 727
Suto Y., Silk J., 1988, ApJ, 326, 527
Tegmark M., Silk J., Rees M. J., Blanchard A., Abel T., Palla F., 1997, ApJ, 474, 1
Thoul A. A., Weinberg D. H., 1995, ApJ, 442, 480
Turner J., Kirby-Docken K., Dalgarno A., 1977, ApJS, 35, 281
Uehara H., Inutsuka S., 2000, ApJ, 531, L91
Wolfire M. G., Cassinelli J. P., 1987, ApJ, 319, 850
Yahil A., 1983, ApJ, 265, 1047

APPENDIX A: THE CODE

Hereafter we describe the main features of the code we developed.

A1 Generalities

A1.1 Gas hydrodynamics

Despite the cosmological context of our calculations, the collapsing baryon clouds we are studying are assumed to be self-gravitating, and we can neglect the gravitational effects of the host dark matter halo.

The code integrates the following 1D Lagrangian hydrodynamical equations (conservation of mass, momentum and energy) using an explicit finite-difference scheme:

$$\frac{\mathrm{d}M_\mathrm{r}}{\mathrm{d}r} = 4\pi r^2 \rho \tag{A1}$$

$$\frac{\mathrm{d}v}{\mathrm{d}t} = -4\pi r^2 \frac{\mathrm{d}p}{\mathrm{d}M_\mathrm{r}} - \frac{GM_r}{r^2} + f_\mathrm{rad} \tag{A2}$$

$$\frac{\mathrm{d}u}{\mathrm{d}t} = -p\frac{\mathrm{d}}{\mathrm{d}t}\left(\frac{1}{\rho}\right) + \frac{\Gamma - \Lambda}{\rho}, \tag{A3}$$

where the Lagrangian coordinate M_r is the mass inside a radius r. ρ, v, p, f_rad, u, represent the density, velocity, pressure, radiative force per unit mass and internal energy per unit mass, respectively. Γ and Λ are the heating and cooling rate per unit volume, respectively.

Hydrodynamical effects are included by adding to the pressure an artificial viscosity term of the form

$$q \propto \rho \Delta v^2, \tag{A4}$$

in regions where contiguous gas shells would self-cross (e.g. Bowers & Wilson 1991; Thoul & Weinberg 1995; hereafter TW95).

A1.2 Chemistry

Because of the extremely low metallicity of the primordial material as predicted by standard big-bang nucleosynthesis ($Z \sim 10^{-12}$; Kolb & Turner 1990), we can safely limit our treatment of chemistry to the various ionic species of atomic hydrogen (H^0, H^+, H^-), molecular hydrogen (H_2, H_2^+) and helium (He^0, He^+, He^{++}), plus free electrons (e^-).

The He number abundance is taken to be 1/12 of the total H number abundance; this translates into mass fractions of $X = 0.75$, $Y = 0.25$ and $Z = 0$.

Some authors (Flower 2000; Flower & Pineau de Forêts 2001; and also, in a different context, Uehara & Inutsuka 2000) suggested that deuterium is an important coolant in a metal-free gas, because of the permanent dipole moment of HD molecules and their low excitation temperature (~ 160 K for HD instead of ~ 510 K for H_2). However, HD cooling is likely to be important only at temperatures below a few hundred degrees, i.e. during the formation of protostellar clouds, rather than during their collapse. For this reason, we neglect the effects of deuterium. Note that BCL01 included HD cooling in their investigation of primordial cloud

Table A1. Chemical reactions and reaction rates.

Reaction		Rate
$H^+ + e^- \rightarrow$	$H + \gamma$	AANZ98, k_2
$H + e^- \rightarrow$	$H^- + \gamma$	AANZ98, k_7
$H + H^- \rightarrow$	$H_2 + e^-$	AANZ98, k_8
$H + H + H \rightarrow$	$H_2 + H$	PSS83, k_4
$H_2 + H \rightarrow$	$H + H + H$	PSS83, k_5
$H + H + H_2 \rightarrow$	$H_2 + H_2$	PSS83, k_6
$H_2 + H_2 \rightarrow$	$H + H + H_2$	PSS83, k_7
$H + e^- \rightarrow$	$H^+ + e^- + e^-$	AANZ98, k_1
$H + H \rightarrow$	$H^+ + H + e^-$	PSS83, k_9

AANZ98 stands for Abel et al. (1998) and PSS83 stands for Palla et al. (1983). Note that the H recombination rate (first reaction in the list) is appropriate for case A (case B could be more appropriate, but results are not affected by the difference, as can be seen from the comparison with ON98).

fragmentation, and found that (for a standard deuterium abundance) the thermal evolution of the gas would not change significantly.

Initial conditions were chosen with chemical abundances far from equilibrium, and we follow their evolution by integrating a network of reactions (see Table A1). In particular, we include the three-body reactions described by Palla et al. (1983).

As the gas gets denser ($\rho \gtrsim \rho_{\rm eq} \equiv 5 \times 10^{-11}\,{\rm g\,cm^{-3}}$), the abundances of the relevant species (H_2, H^0 and He^0, which then represent more than 99.9 per cent of the total number abundance) are close to their equilibrium values, as reactions. We then switch to the equilibrium chemistry.

When the gas is almost ideal, i.e. when $p \leq 10^4\,{\rm dyne\,cm^{-2}}$ (p is the gas pressure) we find the equilibrium abundances by solving the Saha equations for the relevant species. However, these equations become inappropriate at high temperatures and densities, so when $p \geq 10^6\,{\rm dyne\,cm^{-2}}$ we interpolate the abundance values from the tables given by SCVH95. In the intermediate regime ($10^4 \leq p \leq 10^6\,{\rm dyne\,cm^{-2}}$), we evaluate the chemical composition both with the Saha equations and using the SCVH95 tables, and then we interpolate appropriately the two results; this is done in order to ensure a smooth transition between the two regimes.

A1.3 Thermodynamical properties

For the solution of the hydrodynamical equations, we need to specify the equation of state and to calculate the internal energy as a function of temperature, density and chemical composition.

At low densities and temperatures (in practice, we use $p \leq 10^4\,{\rm dyne\,cm^{-2}}$ as a criterion), the gas is ideal to a very good level of approximation and we can use the usual equation

$$p = nkT, \tag{A5}$$

where n is the number density of the gas.

In this ideal regime we can also write the total internal energy per unit mass as

$$u = u_{\rm th} + u_{\rm chem} \tag{A6}$$

with

$$u_{\rm th} = \frac{1}{\gamma_{\rm ad} - 1} N_{\rm tot} kT, \tag{A7}$$

$$u_{\rm chem} = -N_{\rm tot} \sum_{i=1}^{9} y_i \chi_i, \tag{A8}$$

where $u_{\rm th}$ and $u_{\rm chem}$ are the thermal and the chemical energy per unit mass, while $N_{\rm tot}$, y_i and χ_i are the total number of particles per unit mass, the number fraction of particles of species i ($y_i = N_i/N_{\rm tot}$), and the binding energy of a particle of species i, respectively. Finally, $\gamma_{\rm ad}$ is the mean adiabatic index of the gas, obtained by a weighted average of the adiabatic indexes of the various chemical species: for the seven included monoatomic species we have $\gamma_{\rm ad,X} = 5/3$, while for the two diatomic species we use $\gamma_{\rm ad,H_2^+} = 7/5$ and the expression (from ON98) is

$$\frac{1}{\gamma_{\rm ad,H_2} - 1} = \frac{5}{2} + x^2 \frac{{\rm e}^x}{({\rm e}^x - 1)^2}, \quad x = \frac{6100\,{\rm K}}{T}. \tag{A9}$$

The value of γ for H_2^+ neglects the vibrational degrees of freedom, but the abundance of this ion is always very small and this does not introduce any significant error.

When the gas is no longer ideal ($p \geq 10^6\,{\rm dyne\,cm^{-2}}$), we find $p(\rho, T)$ and $u(\rho, T)$ by interpolating the values tabulated by SCVH95, which have been calculated taking non-ideal effects into account. In the transition between the two regimes, we interpolate the results of the ideal and of the SCVH95 values in order to obtain a smooth transition.

A1.4 Radiative transfer and cooling

In the initial stages of collapse, gas cooling is dominated by the H_2 roto-vibrational transitions, which soon become optically thick. A careful treatment of radiative transfer effects is then crucial in the study of the collapse.

H_2 line cooling is important only when $T \lesssim 2500\,{\rm K}$, as at higher temperatures H_2 molecules slowly dissociate, and continuum emission starts dominating the local cooling. The energy gaps between H_2 rotational levels typically correspond to excitation temperatures of few $\times\,100\,{\rm K} - 10^3\,{\rm K}$, while the gap between vibrational levels corresponds to $\sim 6000\,{\rm K}$. Under such conditions, it is adequate to consider only H_2 roto-vibrational levels with rotational quantum number $0 \leq J \leq 20$, and vibrational quantum number $0 \leq v \leq 2$. In this way, all the states whose excitation temperatures (relative to the ground state) is $\lesssim 20\,000\,{\rm K}$ are considered. We treat the radiative transfer of all the lines (between the considered levels) permitted by the quadrupole selection rules.

Line opacities are computed using the Einstein A coefficients from Turner, Kirby-Docken & Dalgarno (1977), and assuming local thermodynamic equilibrium for estimating the level populations. This is correct since the density at which a line gives a relevant contribution to the total cooling is always greater than the critical density at which collisional de-excitations dominate upon radiative transitions.

Finally, the effects of thermal broadening and Doppler shifts due to bulk motions arising in the collapse phase have been included in the line transfer calculations.

When the temperature rises to a sufficiently high value ($T > 1000\,{\rm K}$), we include the cooling by continuum radiation; continuum radiative transfer is treated as a grey problem, using the mean Planck opacity for $Z = 0$ gas from Lenzuni, Chernoff & Salpeter (1991) when $1000\ K < T < 7000\,{\rm K}$, and the Rosseland mean opacity for metal-free gas from Rogers & Iglesias (1992) when $T > 7000\,{\rm K}$.

A2 Numerical details

A2.1 Implementation of the basic equations

The numerical treatment of the dynamical evolution is made along

Table B1. Line list.

$(v_i, J_i) \rightarrow (v_f, J_f)$	λ (μm)	τ	L_{650}	L_{1000}	L_{1500}	$L_{\tau_c=1}$	$l_{\tau_c=1}$
(2,11) → (0,9)	1.0700	4.39×10^{1}	9.91×10^{24}	1.59×10^{29}	6.50×10^{31}	4.55×10^{32}	9.77×10^{22}
(2,10) → (0,8)	1.0701	7.65×10^{1}	7.00×10^{25}	6.32×10^{29}	1.54×10^{32}	6.50×10^{32}	1.40×10^{23}
(2,12) → (0,10)	1.0736	2.34×10^{1}	1.24×10^{24}	3.64×10^{28}	2.36×10^{31}	2.85×10^{32}	6.13×10^{22}
(2,9) → (0,7)	1.0737	1.24×10^{2}	4.32×10^{26}	2.25×10^{30}	2.97×10^{32}	9.08×10^{32}	2.26×10^{23}
(2,8) → (0,6)	1.0806	1.83×10^{2}	2.25×10^{27}	6.99×10^{30}	4.84×10^{32}	1.19×10^{33}	2.97×10^{23}
(2,13) → (0,11)	1.0809	1.18×10^{1}	1.43×10^{23}	7.73×10^{27}	8.01×10^{30}	1.76×10^{32}	3.48×10^{22}
(2,7) → (0,5)	1.0908	2.46×10^{2}	9.68×10^{27}	1.85×10^{31}	6.81×10^{32}	1.44×10^{33}	3.65×10^{23}
(2,14) → (0,12)	1.0925	5.57×10^{0}	1.55×10^{22}	1.54×10^{27}	2.58×10^{30}	1.05×10^{32}	2.09×10^{22}
(2,6) → (0,4)	1.1042	2.98×10^{2}	3.36×10^{28}	3.91×10^{31}	8.61×10^{32}	1.67×10^{33}	4.26×10^{23}
(2,15) → (0,13)	1.1087	2.51×10^{0}	1.61×10^{21}	2.97×10^{26}	7.98×10^{29}	5.79×10^{31}	1.18×10^{22}
(2,5) → (0,3)	1.1210	3.19×10^{2}	9.17×10^{28}	6.66×10^{31}	1.02×10^{33}	1.89×10^{33}	4.91×10^{23}
(2,16) → (0,14)	1.1300	1.07×10^{0}	1.65×10^{20}	5.53×10^{25}	2.38×10^{29}	2.80×10^{31}	5.79×10^{21}
(2,4) → (0,2)	1.1410	2.96×10^{2}	1.90×10^{29}	9.34×10^{31}	1.19×10^{33}	2.06×10^{33}	5.45×10^{23}
(2,17) → (0,15)	1.1573	0.43×10^{0}	1.69×10^{19}	1.00×10^{25}	6.79×10^{28}	1.19×10^{31}	2.52×10^{21}
(2,3) → (0,1)	1.1645	2.27×10^{2}	2.81×10^{29}	1.09×10^{32}	1.29×10^{33}	2.20×10^{33}	5.93×10^{23}
(2,2) → (0,0)	1.1914	1.25×10^{2}	2.59×10^{29}	9.28×10^{31}	1.24×10^{33}	2.13×10^{33}	5.88×10^{23}
(2,18) → (0,16)	1.1915	0.16×10^{0}	1.78×10^{18}	1.81×10^{24}	1.89×10^{28}	4.54×10^{30}	9.91×10^{20}
(2,19) → (0,17)	1.2338	5.57×10^{-2}	1.88×10^{17}	3.14×10^{23}	4.87×10^{27}	1.55×10^{30}	3.49×10^{20}
(2,1) → (0,1)	1.2400	1.20×10^{2}	3.59×10^{29}	1.17×10^{32}	1.47×10^{33}	2.44×10^{33}	7.01×10^{23}
(2,2) → (0,2)	1.2439	1.23×10^{2}	2.69×10^{29}	1.02×10^{32}	1.44×10^{33}	2.46×10^{33}	7.08×10^{23}
(2,3) → (0,3)	1.2498	1.31×10^{2}	1.78×10^{29}	8.42×10^{31}	1.37×10^{33}	2.40×10^{33}	6.94×10^{23}
(2,4) → (0,4)	1.2577	1.24×10^{2}	9.04×10^{28}	5.69×10^{31}	1.23×10^{33}	2.24×10^{33}	6.53×10^{23}
(2,5) → (0,5)	1.2676	1.06×10^{2}	3.60×10^{28}	3.13×10^{31}	1.00×10^{33}	2.01×10^{33}	5.89×10^{23}
(2,6) → (0,6)	1.2796	8.25×10^{1}	1.14×10^{28}	1.45×10^{31}	7.18×10^{32}	1.67×10^{33}	4.30×10^{23}
(2,20) → (0,18)	1.2860	1.58×10^{-2}	1.88×10^{16}	4.89×10^{22}	1.08×10^{27}	4.39×10^{29}	1.03×10^{20}
(2,7) → (0,7)	1.2938	6.00×10^{1}	2.99×10^{27}	5.78×10^{30}	4.51×10^{32}	1.30×10^{33}	3.37×10^{23}
(2,0) → (0,2)	1.2947	6.98×10^{1}	2.58×10^{29}	8.42×10^{31}	1.30×10^{33}	2.28×10^{33}	6.82×10^{23}
(2,8) → (0,8)	1.3101	4.04×10^{1}	6.45×10^{26}	2.01×10^{30}	2.38×10^{32}	9.45×10^{32}	2.49×10^{23}
(2,9) → (0,9)	1.3287	2.59×10^{1}	1.20×10^{26}	6.24×10^{29}	1.10×10^{32}	6.46×10^{32}	1.72×10^{23}
(2,1) → (0,3)	1.3372	8.54×10^{1}	2.76×10^{29}	9.68×10^{31}	1.52×10^{33}	2.65×10^{33}	8.19×10^{23}
(2,10) → (0,10)	1.3497	1.57×10^{1}	1.94×10^{25}	1.75×10^{29}	4.64×10^{31}	4.30×10^{32}	1.16×10^{23}
(2,11) → (0,11)	1.3730	9.12×10^{0}	2.80×10^{24}	4.50×10^{28}	1.85×10^{31}	2.68×10^{32}	6.74×10^{22}
(2,2) → (0,4)	1.3838	7.50×10^{1}	1.81×10^{29}	7.26×10^{31}	1.42×10^{33}	2.52×10^{33}	8.08×10^{23}
(2,12) → (0,12)	1.3988	5.14×10^{0}	3.72×10^{23}	1.09×10^{28}	7.05×10^{30}	1.70×10^{32}	4.35×10^{22}
(2,13) → (0,13)	1.4271	2.81×10^{0}	4.64×10^{22}	2.50×10^{27}	2.59×10^{30}	9.89×10^{31}	2.58×10^{22}
(2,3) → (0,5)	1.4349	5.51×10^{1}	8.39×10^{28}	4.11×10^{31}	1.08×10^{33}	2.13×10^{33}	6.14×10^{23}
(2,14) → (0,14)	1.4581	1.51×10^{0}	5.63×10^{21}	5.62×10^{26}	9.38×10^{29}	5.56×10^{31}	1.48×10^{22}
(2,4) → (0,6)	1.4903	3.49×10^{1}	2.88×10^{28}	1.82×10^{31}	6.56×10^{32}	1.55×10^{33}	4.65×10^{23}
(2,15) → (0,15)	1.4918	0.81×10^{0}	6.88×10^{20}	1.26×10^{26}	3.40×10^{29}	3.01×10^{31}	8.22×10^{21}
(2,16) → (0,16)	1.5283	0.44×10^{0}	8.69×10^{19}	2.90×10^{25}	1.25×10^{29}	1.59×10^{31}	4.46×10^{21}
(2,5) → (0,7)	1.5503	1.97×10^{1}	7.54×10^{27}	6.56×10^{30}	3.12×10^{32}	1.01×10^{33}	3.14×10^{23}
(2,17) → (0,17)	1.5676	0.24×10^{0}	1.17×10^{19}	6.96×10^{24}	4.72×10^{28}	8.39×10^{30}	2.41×10^{21}
(2,18) → (0,18)	1.6097	0.14×10^{0}	1.76×10^{18}	1.79×10^{24}	1.86×10^{28}	4.49×10^{30}	1.32×10^{21}
(2,6) → (0,8)	1.6146	9.92×10^{0}	1.54×10^{27}	1.94×10^{30}	1.21×10^{32}	5.81×10^{32}	1.88×10^{23}
(2,19) → (0,19)	1.6546	7.92×10^{-2}	3.03×10^{17}	5.08×10^{23}	7.86×10^{27}	2.50×10^{30}	7.57×10^{20}
(2,7) → (0,9)	1.6830	4.58×10^{0}	2.51×10^{26}	4.85×10^{29}	4.12×10^{31}	2.90×10^{32}	8.93×10^{22}
(1,13) → (0,11)	1.6989	9.37×10^{0}	2.45×10^{25}	1.66×10^{29}	3.55×10^{31}	3.58×10^{32}	1.11×10^{23}
(1,12) → (0,10)	1.7019	3.36×10^{1}	4.43×10^{26}	1.54×10^{30}	2.01×10^{32}	9.96×10^{32}	3.40×10^{23}
(2,20) → (0,20)	1.7022	4.86×10^{-2}	6.29×10^{16}	1.64×10^{23}	3.60×10^{27}	1.47×10^{30}	4.57×10^{20}
(1,14) → (0,12)	1.7048	1.58×10^{0}	8.06×10^{23}	1.07×10^{28}	3.79×10^{30}	8.03×10^{31}	2.51×10^{22}
(1,11) → (0,9)	1.7134	9.49×10^{1}	6.07×10^{27}	1.10×10^{31}	8.47×10^{32}	2.21×10^{33}	7.61×10^{23}
(1,15) → (0,13)	1.7203	2.19×10^{-2}	2.19×10^{21}	5.67×10^{25}	3.35×10^{28}	1.12×10^{30}	3.52×10^{20}
(1,10) → (0,8)	1.7331	2.25×10^{2}	6.57×10^{28}	6.38×10^{31}	2.43×10^{33}	4.32×10^{33}	1.73×10^{24}
(1,16) → (0,14)	1.7464	0.23×10^{0}	4.68×10^{21}	2.34×10^{26}	2.28×10^{29}	1.07×10^{31}	3.42×10^{21}
(2,8) → (0,10)	1.7552	1.92×10^{0}	3.29×10^{25}	1.02×10^{29}	1.23×10^{31}	1.27×10^{32}	4.08×10^{22}
(1,9) → (0,7)	1.7610	4.66×10^{2}	5.76×10^{29}	3.09×10^{32}	5.01×10^{33}	7.29×10^{33}	2.97×10^{24}
(1,17) → (0,15)	1.7847	0.65×10^{0}	2.76×10^{21}	2.60×10^{26}	4.15×10^{29}	2.62×10^{31}	8.55×10^{21}
(1,8) → (0,6)	1.7974	8.55×10^{2}	4.05×10^{30}	1.16×10^{33}	8.32×10^{33}	1.13×10^{34}	4.72×10^{24}
(2,12) → (1,10)	1.8248	2.55×10^{0}	1.85×10^{23}	5.41×10^{27}	3.51×10^{30}	1.02×10^{32}	3.39×10^{22}
(2,13) → (1,11)	1.8259	0.40×10^{0}	6.58×10^{21}	3.55×10^{26}	3.68×10^{29}	1.77×10^{31}	5.93×10^{21}
(2,9) → (0,11)	1.8302	0.75×10^{0}	3.60×10^{24}	1.87×10^{28}	3.30×10^{30}	4.74×10^{31}	1.59×10^{22}
(2,11) → (1,9)	1.8333	8.88×10^{0}	2.76×10^{24}	4.44×10^{28}	1.82×10^{31}	2.81×10^{32}	9.42×10^{22}
(2,14) → (1,12)	1.8371	1.74×10^{-4}	6.35×10^{17}	6.33×10^{22}	1.06×10^{26}	7.16×10^{27}	2.41×10^{18}
(1,18) → (0,16)	1.8372	0.89×10^{0}	8.63×10^{20}	1.48×10^{26}	3.77×10^{29}	3.20×10^{31}	1.08×10^{22}
(1,7) → (0,5)	1.8426	1.39×10^{3}	2.26×10^{31}	3.04×10^{33}	1.26×10^{34}	1.55×10^{34}	8.12×10^{24}
(2,10) → (1,8)	1.8511	2.34×10^{1}	2.96×10^{25}	2.67×10^{29}	7.08×10^{31}	6.21×10^{32}	2.31×10^{23}
(2,15) → (1,13)	1.8595	0.13×10^{0}	1.03×10^{20}	1.90×10^{25}	5.11×10^{28}	4.80×10^{30}	1.64×10^{21}
(2,9) → (1,7)	1.8780	5.15×10^{1}	2.45×10^{26}	1.28×10^{30}	2.25×10^{32}	1.18×10^{33}	4.44×10^{23}
(2,16) → (1,14)	1.8944	0.31×10^{0}	5.73×10^{19}	1.91×10^{25}	8.24×10^{28}	1.06×10^{31}	3.69×10^{21}
(1,6) → (0,4)	1.8971	1.99×10^{3}	9.77×10^{31}	5.83×10^{33}	1.68×10^{34}	2.01×10^{34}	1.09×10^{25}
(1,19) → (0,17)	1.9070	0.97×10^{0}	2.37×10^{20}	7.08×10^{25}	2.79×10^{29}	3.16×10^{31}	1.10×10^{22}

Table B1 – *continued*

$(v_i, J_i) \rightarrow (v_f, J_f)$	λ (μm)	τ	L_{650}	L_{1000}	L_{1500}	$L_{\tau_c=1}$	$l_{\tau_c=1}$
(2,10) → (0,12)	1.9071	0.27×10^{0}	3.32×10^{23}	3.00×10^{27}	7.96×10^{29}	1.55×10^{31}	5.42×10^{21}
(2,8) → (1,6)	1.9142	9.77×10^{1}	1.61×10^{27}	5.00×10^{30}	5.94×10^{32}	2.02×10^{33}	7.78×10^{23}
(2,17) → (1,15)	1.9439	0.41×10^{0}	1.85×10^{19}	1.10×10^{25}	7.45×10^{28}	1.31×10^{31}	4.65×10^{21}
(2,7) → (1,5)	1.9600	1.62×10^{2}	8.29×10^{27}	1.61×10^{31}	1.27×10^{33}	3.06×10^{33}	1.20×10^{24}
(1,5) → (0,3)	1.9617	2.51×10^{3}	3.21×10^{32}	9.35×10^{33}	2.20×10^{34}	2.55×10^{34}	1.43×10^{25}
(2,11) → (0,13)	1.9845	8.94×10^{-2}	2.65×10^{22}	4.27×10^{26}	1.75×10^{29}	4.59×10^{30}	1.67×10^{21}
(1,20) → (0,18)	1.9985	0.95×10^{0}	6.70×10^{19}	3.30×10^{25}	1.93×10^{29}	2.87×10^{31}	1.05×10^{22}
(2,18) → (1,16)	2.0108	0.44×10^{0}	5.19×10^{18}	5.29×10^{24}	5.51×10^{28}	1.30×10^{31}	4.79×10^{21}
(2,6) → (1,4)	2.0160	2.35×10^{2}	3.34×10^{28}	4.23×10^{31}	2.21×10^{33}	4.37×10^{33}	2.04×10^{24}
(1,4) → (0,2)	2.0372	2.70×10^{3}	7.62×10^{32}	1.28×10^{34}	2.68×10^{34}	2.95×10^{34}	1.71×10^{25}
(2,12) → (0,14)	2.0602	2.80×10^{-2}	1.88×10^{21}	5.50×10^{25}	3.57×10^{28}	1.27×10^{30}	4.78×10^{20}
(2,5) → (1,3)	2.0829	2.98×10^{2}	1.03×10^{29}	8.95×10^{31}	3.17×10^{33}	5.33×10^{33}	2.57×10^{24}
(2,19) → (1,17)	2.0994	0.43×10^{0}	1.45×10^{18}	2.43×10^{24}	3.76×10^{28}	1.17×10^{31}	4.51×10^{21}
(1,3) → (0,1)	2.1249	2.40×10^{3}	1.28×10^{33}	1.62×10^{34}	3.05×10^{34}	3.40×10^{34}	2.06×10^{25}
(2,13) → (0,15)	2.1320	8.21×10^{-3}	1.21×10^{20}	6.52×10^{24}	6.76×10^{27}	3.31×10^{29}	1.29×10^{20}
(2,4) → (1,2)	2.1617	3.25×10^{2}	2.36×10^{29}	1.49×10^{32}	3.97×10^{33}	6.30×10^{33}	3.15×10^{24}
(2,14) → (0,16)	2.1968	2.27×10^{-3}	7.26×10^{18}	7.25×10^{23}	1.21×10^{27}	8.20×10^{28}	3.30×10^{19}
(2,20) → (1,18)	2.2155	0.41×10^{0}	4.45×10^{17}	1.16×10^{24}	2.55×10^{28}	1.02×10^{31}	4.13×10^{21}
(1,2) → (0,0)	2.2261	1.54×10^{3}	1.33×10^{33}	1.67×10^{34}	3.19×10^{34}	3.53×10^{34}	2.24×10^{25}
(2,15) → (0,17)	2.2514	6.02×10^{-4}	4.22×10^{17}	7.76×10^{22}	2.09×10^{26}	1.96×10^{28}	8.10×10^{18}
(2,3) → (1,1)	2.2537	2.91×10^{2}	3.81×10^{29}	1.86×10^{32}	4.20×10^{33}	6.44×10^{33}	3.36×10^{24}
(2,16) → (0,18)	2.2922	1.55×10^{-4}	2.48×10^{16}	8.29×10^{21}	3.57×10^{25}	4.64×10^{27}	1.95×10^{18}
(2,17) → (0,19)	2.3159	4.12×10^{-5}	1.60×10^{15}	9.48×10^{20}	6.42×10^{24}	1.15×10^{27}	4.86×10^{17}
(2,18) → (0,20)	2.3196	1.26×10^{-5}	1.29×10^{14}	1.32×10^{20}	1.37×10^{24}	3.31×10^{26}	1.40×10^{17}
(2,2) → (1,0)	2.3603	1.88×10^{2}	3.78×10^{29}	1.52×10^{32}	3.38×10^{33}	5.33×10^{33}	2.91×10^{24}
(1,1) → (0,1)	2.4094	1.82×10^{3}	2.04×10^{33}	2.21×10^{34}	3.90×10^{34}	4.26×10^{34}	2.92×10^{25}
(1,2) → (0,2)	2.4165	1.85×10^{3}	1.49×10^{33}	2.04×10^{34}	3.64×10^{34}	3.98×10^{34}	2.74×10^{25}
(1,3) → (0,3)	2.4273	1.92×10^{3}	9.28×10^{32}	1.77×10^{34}	3.41×10^{34}	3.76×10^{34}	2.60×10^{25}
(1,4) → (0,4)	2.4416	1.78×10^{3}	4.34×10^{32}	1.36×10^{34}	3.03×10^{34}	3.27×10^{34}	2.27×10^{25}
(1,5) → (0,5)	2.4597	1.49×10^{3}	1.56×10^{32}	9.01×10^{33}	2.37×10^{34}	2.72×10^{34}	1.91×10^{25}
(1,6) → (0,6)	2.4815	1.13×10^{3}	4.37×10^{31}	4.65×10^{33}	1.81×10^{34}	2.08×10^{34}	1.20×10^{25}
(1,7) → (0,7)	2.5071	7.88×10^{2}	9.81×10^{30}	1.81×10^{33}	1.19×10^{34}	1.46×10^{34}	8.49×10^{24}
(1,8) → (0,8)	2.5366	5.12×10^{2}	1.81×10^{30}	5.59×10^{32}	7.21×10^{33}	9.57×10^{33}	5.62×10^{24}
(2,1) → (1,1)	2.5547	2.26×10^{2}	5.72×10^{29}	2.02×10^{32}	3.92×10^{33}	5.77×10^{33}	3.41×10^{24}
(2,2) → (1,2)	2.5633	2.34×10^{2}	4.26×10^{29}	1.71×10^{32}	3.74×10^{33}	5.77×10^{33}	3.42×10^{24}
(1,9) → (0,9)	2.5701	3.13×10^{2}	2.81×10^{29}	1.51×10^{32}	3.84×10^{33}	5.84×10^{33}	3.47×10^{24}
(2,3) → (1,3)	2.5763	2.46×10^{2}	2.76×10^{29}	1.35×10^{32}	3.41×10^{33}	5.40×10^{33}	3.22×10^{24}
(2,4) → (1,4)	2.5937	2.32×10^{2}	1.37×10^{29}	8.68×10^{31}	2.80×10^{33}	4.59×10^{33}	2.76×10^{24}
(1,10) → (0,10)	2.6077	1.80×10^{2}	3.72×10^{28}	3.60×10^{31}	1.71×10^{33}	3.49×10^{33}	1.83×10^{24}
(2,5) → (1,5)	2.6156	1.98×10^{2}	5.31×10^{28}	4.62×10^{31}	1.99×10^{33}	3.72×10^{33}	1.95×10^{24}
(1,0) → (0,2)	2.6297	1.32×10^{3}	1.63×10^{33}	2.18×10^{34}	3.79×10^{34}	4.11×10^{34}	3.08×10^{25}
(2,6) → (1,6)	2.6421	1.54×10^{2}	1.64×10^{28}	2.07×10^{31}	1.24×10^{33}	2.90×10^{33}	1.54×10^{24}
(1,11) → (0,11)	2.6495	9.92×10^{1}	4.37×10^{27}	7.92×10^{30}	6.37×10^{32}	1.91×10^{33}	1.02×10^{24}
(2,7) → (1,7)	2.6735	1.11×10^{2}	4.09×10^{27}	7.93×10^{30}	6.68×10^{32}	1.99×10^{33}	1.07×10^{24}
(1,12) → (0,12)	2.6955	5.26×10^{1}	4.64×10^{26}	1.61×10^{30}	2.11×10^{32}	9.93×10^{32}	5.37×10^{23}
(2,8) → (1,8)	2.7097	7.41×10^{1}	8.51×10^{26}	2.65×10^{30}	3.18×10^{32}	1.28×10^{33}	6.94×10^{23}
(1,13) → (0,13)	2.7459	2.71×10^{1}	4.60×10^{25}	3.11×10^{29}	6.67×10^{31}	5.20×10^{32}	2.87×10^{23}
(2,9) → (1,9)	2.7510	4.68×10^{1}	1.50×10^{26}	7.81×10^{29}	1.38×10^{32}	8.02×10^{32}	4.43×10^{23}
(2,0) → (1,2)	2.7891	1.69×10^{2}	4.45×10^{29}	1.47×10^{32}	2.99×10^{33}	4.57×10^{33}	2.95×10^{24}
(2,10) → (1,10)	2.7976	2.81×10^{1}	2.31×10^{25}	2.08×10^{29}	5.52×10^{31}	4.79×10^{32}	2.69×10^{23}
(1,14) → (0,14)	2.8008	1.36×10^{1}	4.37×10^{24}	5.79×10^{28}	2.06×10^{31}	2.71×10^{32}	1.39×10^{23}
(1,1) → (0,3)	2.8057	1.87×10^{3}	1.77×10^{33}	2.49×10^{34}	4.22×10^{34}	4.55×10^{34}	3.64×10^{25}
(2,11) → (1,11)	2.8498	1.60×10^{1}	3.14×10^{24}	5.04×10^{28}	2.07×10^{31}	2.76×10^{32}	1.44×10^{23}
(1,15) → (0,15)	2.8601	6.79×10^{0}	4.14×10^{23}	1.07×10^{28}	6.34×10^{30}	1.40×10^{32}	7.35×10^{22}
(2,12) → (1,12)	2.9077	8.82×10^{0}	3.90×10^{23}	1.14×10^{28}	7.39×10^{30}	1.62×10^{32}	8.63×10^{22}
(1,16) → (0,16)	2.9240	3.39×10^{0}	4.03×10^{22}	2.01×10^{27}	1.97×10^{30}	7.09×10^{31}	3.80×10^{22}
(2,13) → (1,13)	2.9716	4.73×10^{0}	4.56×10^{22}	2.46×10^{27}	2.55×10^{30}	8.82×10^{31}	4.80×10^{22}
(2,1) → (1,3)	2.9774	2.44×10^{2}	4.94×10^{29}	1.74×10^{32}	3.51×10^{33}	5.26×10^{33}	3.62×10^{24}
(1,17) → (0,17)	2.9923	1.70×10^{0}	4.16×10^{21}	3.92×10^{26}	6.26×10^{29}	3.57×10^{31}	1.96×10^{22}
(1,2) → (0,4)	3.0073	1.92×10^{3}	1.16×10^{33}	2.24×10^{34}	3.94×10^{34}	4.24×10^{34}	3.64×10^{25}
(2,14) → (1,14)	3.0417	2.50×10^{0}	5.17×10^{21}	5.16×10^{26}	8.61×10^{29}	4.72×10^{31}	2.63×10^{22}
(1,18) → (0,18)	3.0651	0.88×10^{0}	4.78×10^{20}	8.20×10^{25}	2.09×10^{29}	1.78×10^{31}	10.00×10^{21}
(2,15) → (1,15)	3.1184	1.30×10^{0}	5.80×10^{20}	1.07×10^{26}	2.87×10^{29}	2.43×10^{31}	1.39×10^{22}
(1,19) → (0,19)	3.1422	0.47×10^{0}	6.28×10^{19}	1.88×10^{25}	7.40×10^{28}	8.86×10^{30}	5.10×10^{21}
(2,2) → (1,4)	3.1941	2.56×10^{2}	3.35×10^{29}	1.35×10^{32}	3.07×10^{33}	4.63×10^{33}	3.42×10^{24}
(2,16) → (1,16)	3.2018	0.68×10^{0}	6.72×10^{19}	2.25×10^{25}	9.66×10^{28}	1.20×10^{31}	7.05×10^{21}
(1,20) → (0,20)	3.2232	0.26×10^{0}	9.88×10^{18}	4.86×10^{24}	2.84×10^{28}	4.55×10^{30}	2.69×10^{21}
(1,3) → (0,5)	3.2385	1.65×10^{3}	5.24×10^{32}	1.61×10^{34}	3.22×10^{34}	3.37×10^{34}	3.11×10^{25}
(2,17) → (1,17)	3.2923	0.36×10^{0}	8.30×10^{18}	4.92×10^{24}	3.33×10^{28}	5.88×10^{30}	3.54×10^{21}
(2,18) → (1,18)	3.3899	0.19×10^{0}	1.12×10^{18}	1.14×10^{24}	1.19×10^{28}	2.86×10^{30}	1.78×10^{21}
(2,3) → (1,5)	3.4438	2.25×10^{2}	1.59×10^{29}	7.79×10^{31}	2.18×10^{33}	3.57×10^{33}	2.47×10^{24}

Table B1 – *continued*

$(v_i, J_i) \rightarrow (v_f, J_f)$	λ (μm)	τ	L_{650}	L_{1000}	L_{1500}	$L_{\tau_c=1}$	$l_{\tau_c=1}$
(2,19) → (1,19)	3.4948	0.11×10^{0}	1.75×10^{17}	2.93×10^{23}	4.53×10^{27}	1.44×10^{30}	9.22×10^{20}
(1,4) → (0,6)	3.5034	1.22×10^{3}	1.71×10^{32}	8.63×10^{33}	2.22×10^{34}	2.37×10^{34}	1.92×10^{25}
(2,20) → (1,20)	3.6070	6.16×10^{-2}	3.23×10^{16}	8.39×10^{22}	1.85×10^{27}	7.53×10^{29}	4.97×10^{20}
(2,4) → (1,6)	3.7313	1.72×10^{2}	5.56×10^{28}	3.52×10^{31}	1.26×10^{33}	2.37×10^{33}	1.78×10^{24}
(1,5) → (0,7)	3.8063	8.07×10^{2}	4.18×10^{31}	3.29×10^{33}	1.33×10^{34}	1.49×10^{34}	1.31×10^{25}
(2,5) → (1,7)	4.0622	1.18×10^{2}	1.48×10^{28}	1.29×10^{31}	6.06×10^{32}	1.45×10^{33}	1.19×10^{24}
(1,6) → (0,8)	4.1517	4.84×10^{2}	7.87×10^{30}	9.33×10^{32}	6.68×10^{33}	7.78×10^{33}	7.48×10^{24}
(0,15) → (0,13)	4.3167	1.04×10^{3}	5.78×10^{27}	1.71×10^{31}	1.63×10^{33}	3.08×10^{33}	3.08×10^{24}
(0,16) → (0,14)	4.3364	6.68×10^{2}	6.49×10^{26}	3.93×10^{30}	7.34×10^{32}	1.86×10^{33}	1.62×10^{24}
(0,14) → (0,12)	4.3568	1.59×10^{3}	5.08×10^{28}	7.30×10^{31}	3.22×10^{33}	4.75×10^{33}	4.79×10^{24}
(0,17) → (0,15)	4.4219	4.35×10^{2}	7.52×10^{25}	9.09×10^{29}	3.00×10^{32}	1.18×10^{33}	1.05×10^{24}
(2,6) → (1,8)	4.4422	7.29×10^{1}	3.05×10^{27}	3.86×10^{30}	2.40×10^{32}	7.47×10^{32}	6.66×10^{23}
(0,13) → (0,11)	4.4558	2.38×10^{3}	4.26×10^{29}	2.96×10^{32}	5.79×10^{33}	7.21×10^{33}	7.44×10^{24}
(1,7) → (0,9)	4.5431	2.63×10^{2}	1.15×10^{30}	2.15×10^{32}	2.80×10^{33}	3.74×10^{33}	3.93×10^{24}
(0,18) → (0,16)	4.5859	2.89×10^{2}	9.34×10^{24}	2.18×10^{29}	1.19×10^{32}	7.07×10^{32}	6.51×10^{23}
(1,15) → (1,13)	4.6058	1.07×10^{2}	2.65×10^{24}	6.86×10^{28}	4.05×10^{31}	3.80×10^{32}	3.52×10^{23}
(0,12) → (0,10)	4.6173	3.43×10^{3}	3.27×10^{30}	1.11×10^{33}	9.48×10^{33}	1.08×10^{34}	1.16×10^{25}
(1,14) → (1,12)	4.6386	1.58×10^{2}	1.97×10^{25}	2.62×10^{29}	9.29×10^{31}	5.62×10^{32}	5.23×10^{23}
(1,16) → (1,14)	4.6391	7.20×10^{1}	3.55×10^{23}	1.77×10^{28}	1.73×10^{31}	2.43×10^{32}	2.27×10^{23}
(1,13) → (1,11)	4.7356	2.28×10^{2}	1.40×10^{26}	9.44×10^{29}	2.02×10^{32}	8.39×10^{32}	7.98×10^{23}
(1,17) → (1,15)	4.7462	4.87×10^{1}	4.86×10^{22}	4.58×10^{27}	7.31×10^{30}	1.61×10^{32}	1.53×10^{23}
(0,11) → (0,9)	4.8495	4.68×10^{3}	2.20×10^{31}	3.64×10^{33}	1.49×10^{34}	1.65×10^{34}	1.86×10^{25}
(0,19) → (0,17)	4.8513	2.02×10^{2}	1.30×10^{24}	5.58×10^{28}	4.86×10^{31}	4.45×10^{32}	4.33×10^{23}
(2,7) → (1,9)	4.8764	4.10×10^{1}	4.95×10^{26}	9.59×10^{29}	8.15×10^{31}	3.54×10^{32}	3.46×10^{23}
(1,12) → (1,10)	4.8999	3.17×10^{2}	9.11×10^{26}	3.17×10^{30}	4.07×10^{32}	1.13×10^{33}	1.11×10^{24}
(1,18) → (1,16)	4.9429	3.40×10^{1}	7.16×10^{21}	1.23×10^{27}	3.13×10^{30}	1.03×10^{32}	9.32×10^{22}
(2,15) → (2,13)	4.9684	1.31×10^{1}	2.31×10^{21}	4.24×10^{26}	1.14×10^{30}	5.49×10^{31}	4.99×10^{22}
(1,8) → (0,10)	4.9824	1.31×10^{2}	1.35×10^{29}	4.17×10^{31}	9.06×10^{32}	1.52×10^{33}	1.52×10^{24}
(2,14) → (2,12)	4.9894	1.86×10^{1}	1.44×10^{22}	1.44×10^{27}	2.40×10^{30}	7.54×10^{31}	6.89×10^{22}
(2,16) → (2,14)	5.0221	9.20×10^{0}	3.67×10^{20}	1.23×10^{26}	5.27×10^{29}	3.84×10^{31}	3.53×10^{22}
(2,13) → (2,11)	5.0817	2.57×10^{1}	8.60×10^{22}	4.64×10^{27}	4.80×10^{30}	1.02×10^{32}	9.49×10^{22}
(1,11) → (1,9)	5.1400	4.19×10^{2}	5.27×10^{27}	9.57×10^{30}	7.26×10^{32}	1.52×10^{33}	1.57×10^{24}
(2,17) → (2,15)	5.1610	6.57×10^{0}	6.04×10^{19}	3.59×10^{25}	2.43×10^{29}	2.64×10^{31}	2.49×10^{22}
(0,10) → (0,8)	5.1673	5.98×10^{3}	1.26×10^{32}	9.17×10^{33}	2.09×10^{34}	2.29×10^{34}	3.38×10^{25}
(2,12) → (2,10)	5.2478	3.45×10^{1}	4.75×10^{23}	1.39×10^{28}	9.01×10^{30}	1.32×10^{32}	1.40×10^{23}
(1,19) → (1,17)	5.2578	2.45×10^{1}	1.16×10^{21}	3.46×10^{26}	1.36×10^{30}	6.60×10^{31}	6.36×10^{22}
(0,20) → (0,18)	5.2594	1.51×10^{2}	2.09×10^{23}	1.56×10^{28}	2.09×10^{31}	2.70×10^{32}	2.85×10^{23}
(2,8) → (1,10)	5.3686	2.12×10^{1}	6.51×10^{25}	2.02×10^{29}	2.44×10^{31}	1.56×10^{32}	1.69×10^{23}
(2,18) → (2,16)	5.4058	4.82×10^{0}	1.06×10^{19}	1.08×10^{25}	1.13×10^{29}	1.79×10^{31}	1.77×10^{22}
(1,9) → (0,11)	5.4679	6.01×10^{1}	1.29×10^{28}	6.91×10^{30}	2.32×10^{32}	5.77×10^{32}	6.34×10^{23}
(1,10) → (1,8)	5.4711	5.17×10^{2}	2.60×10^{28}	2.52×10^{31}	1.12×10^{33}	1.90×10^{33}	2.40×10^{24}
(2,11) → (2,9)	5.4959	4.40×10^{1}	2.34×10^{24}	3.77×10^{28}	1.55×10^{31}	1.56×10^{32}	1.73×10^{23}
(0,9) → (0,7)	5.5942	6.98×10^{3}	5.82×10^{32}	1.72×10^{34}	2.80×10^{34}	2.97×10^{34}	4.73×10^{25}
(1,20) → (1,18)	5.7428	1.96×10^{1}	2.22×10^{20}	1.09×10^{26}	6.38×10^{29}	4.37×10^{31}	4.60×10^{22}
(2,19) → (2,17)	5.7939	3.71×10^{0}	2.06×10^{18}	3.45×10^{24}	5.34×10^{28}	1.19×10^{31}	1.27×10^{22}
(2,10) → (2,8)	5.8420	5.26×10^{1}	9.91×10^{24}	8.94×10^{28}	2.37×10^{31}	1.86×10^{32}	2.18×10^{23}
(1,9) → (1,7)	5.9180	5.88×10^{2}	1.05×10^{29}	5.61×10^{31}	1.51×10^{33}	2.17×10^{33}	2.97×10^{24}
(2,9) → (1,11)	5.9189	1.01×10^{1}	7.05×10^{24}	3.67×10^{28}	6.46×10^{30}	6.33×10^{31}	6.86×10^{22}
(1,10) → (0,12)	5.9915	2.55×10^{1}	1.03×10^{27}	1.00×10^{30}	5.15×10^{31}	1.98×10^{32}	2.38×10^{23}
(0,8) → (0,6)	6.1682	7.36×10^{3}	2.09×10^{33}	2.61×10^{34}	3.58×10^{34}	3.52×10^{34}	6.19×10^{25}
(2,9) → (2,7)	6.3119	5.83×10^{1}	3.48×10^{25}	1.81×10^{29}	3.19×10^{31}	1.92×10^{32}	2.44×10^{23}
(2,20) → (2,18)	6.3949	3.09×10^{0}	4.59×10^{17}	1.19×10^{24}	2.63×10^{28}	7.87×10^{30}	9.21×10^{21}
(1,8) → (1,6)	6.5205	6.06×10^{2}	3.31×10^{29}	1.02×10^{32}	1.72×10^{33}	2.23×10^{33}	3.36×10^{24}
(2,10) → (1,12)	6.5207	4.46×10^{0}	6.44×10^{23}	5.81×10^{27}	1.54×10^{30}	2.33×10^{31}	2.78×10^{22}
(1,11) → (0,13)	6.5354	9.87×10^{0}	7.05×10^{25}	1.28×10^{29}	1.04×10^{31}	6.46×10^{31}	7.73×10^{22}
(2,8) → (2,6)	6.9478	5.83×10^{1}	9.62×10^{25}	2.99×10^{29}	3.60×10^{31}	1.74×10^{32}	2.43×10^{23}
(0,7) → (0,5)	6.9523	6.86×10^{3}	5.52×10^{33}	3.30×10^{34}	3.87×10^{34}	3.92×10^{34}	7.77×10^{25}
(1,12) → (0,14)	7.0689	3.51×10^{0}	4.23×10^{24}	1.47×10^{28}	1.92×10^{30}	1.95×10^{31}	2.53×10^{22}
(2,11) → (1,13)	7.1563	1.81×10^{0}	5.08×10^{22}	8.17×10^{26}	3.36×10^{29}	7.78×10^{30}	1.02×10^{22}
(1,7) → (1,5)	7.3448	5.49×10^{2}	7.79×10^{29}	1.45×10^{32}	1.66×10^{33}	2.06×10^{33}	3.51×10^{24}
(1,18) → (0,20)	7.3467	4.62×10^{-4}	3.78×10^{16}	6.48×10^{21}	1.65×10^{25}	1.50×10^{27}	2.01×10^{18}
(1,13) → (0,15)	7.5460	1.13×10^{0}	2.28×10^{23}	1.54×10^{27}	3.30×10^{29}	5.28×10^{30}	7.30×10^{21}
(2,12) → (1,14)	7.7921	0.67×10^{0}	3.51×10^{21}	1.03×10^{26}	6.66×10^{28}	2.29×10^{30}	3.27×10^{21}
(1,17) → (0,19)	7.8090	3.27×10^{-3}	9.91×10^{17}	9.33×10^{22}	1.49×10^{26}	9.79×10^{27}	1.40×10^{19}
(2,7) → (2,5)	7.8200	5.17×10^{1}	2.01×10^{26}	3.89×10^{29}	3.31×10^{31}	1.39×10^{32}	2.18×10^{23}
(1,14) → (0,16)	7.9088	0.33×10^{0}	1.14×10^{22}	1.51×10^{26}	5.35×10^{28}	1.26×10^{30}	1.83×10^{21}
(0,6) → (0,4)	8.0563	5.44×10^{3}	9.89×10^{33}	3.48×10^{34}	3.72×10^{34}	3.74×10^{34}	8.58×10^{25}
(1,16) → (0,18)	8.0684	1.81×10^{-2}	2.37×10^{19}	1.18×10^{24}	1.16×10^{27}	5.43×10^{28}	8.02×10^{19}
(1,15) → (0,17)	8.0977	8.27×10^{-2}	5.32×10^{20}	1.38×10^{25}	8.13×10^{27}	2.72×10^{29}	4.03×10^{20}
(2,18) → (1,20)	8.2737	8.43×10^{-5}	6.52×10^{13}	6.64×10^{19}	6.91×10^{23}	1.67×10^{26}	2.52×10^{17}
(2,13) → (1,15)	8.3749	0.22×10^{0}	2.20×10^{20}	1.18×10^{25}	1.23×10^{28}	5.98×10^{29}	9.18×10^{20}

Table B1 – *continued*

$(v_i, J_i) \rightarrow (v_f, J_f)$	λ (μm)	τ	L_{650}	L_{1000}	L_{1500}	$L_{\tau_c=1}$	$l_{\tau_c=1}$
(1,6) → (1,4)	8.5070	4.27×10^{2}	1.28×10^{30}	1.52×10^{32}	1.31×10^{33}	1.56×10^{33}	3.08×10^{24}
(2,17) → (1,19)	8.8069	6.51×10^{-4}	1.61×10^{15}	9.55×10^{20}	6.47×10^{24}	1.15×10^{27}	1.86×10^{18}
(2,14) → (1,16)	8.8339	6.61×10^{-2}	1.27×10^{19}	1.26×10^{24}	2.11×10^{27}	1.43×10^{29}	2.31×10^{20}
(2,6) → (2,4)	9.0514	3.94×10^{1}	2.97×10^{26}	3.75×10^{29}	2.34×10^{31}	9.27×10^{31}	1.68×10^{23}
(2,16) → (1,18)	9.0901	3.72×10^{-3}	3.45×10^{16}	1.15×10^{22}	4.96×10^{25}	6.45×10^{27}	1.07×10^{19}
(2,15) → (1,17)	9.0924	1.71×10^{-2}	6.82×10^{17}	1.25×10^{23}	3.37×10^{26}	3.17×10^{28}	5.29×10^{19}
(0,5) → (0,3)	9.6894	3.54×10^{3}	1.12×10^{34}	2.78×10^{34}	2.90×10^{34}	2.90×10^{34}	7.99×10^{25}
(1,5) → (1,3)	10.2273	2.73×10^{2}	1.35×10^{30}	1.08×10^{32}	7.61×10^{32}	8.85×10^{32}	2.10×10^{24}
(2,5) → (2,3)	10.8762	2.47×10^{1}	2.86×10^{26}	2.49×10^{29}	1.18×10^{31}	4.56×10^{31}	9.96×10^{22}
(0,4) → (0,2)	12.3006	1.75×10^{3}	7.30×10^{33}	1.58×10^{34}	1.55×10^{34}	1.53×10^{34}	5.35×10^{25}
(1,4) → (1,2)	12.9795	1.32×10^{2}	7.97×10^{29}	4.57×10^{31}	2.93×10^{32}	3.39×10^{32}	1.02×10^{24}
(2,4) → (2,2)	13.7974	1.19×10^{1}	1.56×10^{26}	9.89×10^{28}	3.75×10^{30}	1.46×10^{31}	3.69×10^{22}
(0,3) → (0,1)	17.0595	5.63×10^{2}	2.08×10^{33}	4.73×10^{33}	4.58×10^{33}	4.47×10^{33}	2.17×10^{25}
(1,3) → (1,1)	17.9969	4.22×10^{1}	2.03×10^{29}	8.87×10^{30}	5.23×10^{31}	6.75×10^{31}	2.44×10^{23}
(2,3) → (2,1)	19.1253	3.73×10^{0}	3.72×10^{25}	1.82×10^{28}	5.73×10^{29}	2.49×10^{30}	8.72×10^{21}
(0,2) → (0,0)	28.2559	7.90×10^{1}	1.27×10^{32}	3.51×10^{32}	3.63×10^{32}	3.36×10^{32}	2.20×10^{24}
(1,2) → (1,0)	29.8042	5.88×10^{0}	1.12×10^{28}	4.01×10^{29}	2.10×10^{30}	3.35×10^{30}	1.83×10^{22}
(2,2) → (2,0)	31.6666	0.52×10^{0}	1.96×10^{24}	7.89×10^{26}	2.16×10^{28}	9.82×10^{28}	5.69×10^{20}
Sum of lines	–	–	5.32×10^{34}	4.32×10^{35}	8.92×10^{35}	1.06×10^{36}	–
Continuum	–	1.00×10^{0}	–	8.39×10^{27}	1.29×10^{33}	7.50×10^{35}	$\sim 5 \times 10^{21}$
Total	–	–	5.32×10^{34}	4.32×10^{35}	8.93×10^{35}	1.81×10^{36}	–

the lines described by Bowers & Wilson (1991), and TW95. With the exception of the energy equation, the dynamical equations listed in Section 2.1 were discretized as in TW95 (their equations 9–13 and 15), assuming a value of 4 for the artificial viscosity parameter c_q. Such a Lagrangian finite-difference scheme is second order accurate in space and time.

For the energy equation (A3), our treatment starts from equation (14) of TW95. The chemical term in the internal energy (see Section 2.3) introduces a complex dependence upon the final temperature. For this reason the energy equation is solved iteratively, using the bisection method. In this case the result is only first order accurate in time.

A2.2 Time-steps

The integration time-step is chosen by evaluating the minimum among:

(i) twice the previous integration time-step;

(ii) the minimum dynamical time-scale over all shells i, $\min_i[C_{\rm dyn}(Gr_i^3/M_{r,i})^{1/2}]$;

(iii) the minimum Courant time-scale over all shells i, $\min_i(C_{\rm Cour}\Delta r_i/c_{{\rm s},i})$;

(iv) the minimum cooling time-scale over all shells i, $\min_i[C_{\rm cool}u_i\rho/(\Gamma_i - \Lambda_i)]$;

(v) the minimum crossing time-scale over all shells i, $\min_i(C_{\rm cross}\Delta r_i/\Delta v_i)$.

In addition, we check *aposteriori* that the temperature does not change by more than 0.5 per cent in a single time-step. The factors $C_{\rm dyn} = 1$, $C_{\rm Cour} = 0.2$, $C_{\rm cool} = 0.1$ and $C_{\rm cross} = 0.05$ are safety constants.

A2.3 Boundary conditions

As an internal boundary condition we simply require that the centre of our object should be a geometrical point ($r = 0, M_r = M_0 = 0$) with zero velocity ($v_{\rm in} = 0$).

The external boundary condition is set by taking a constant pressure outside the most external shell.

A2.4 Implementation of radiative transfer

General scheme. The solution of the radiative transfer equation in spherical symmetry requires finding the specific intensity $I_\nu(r, \mu)$, where μ is the cosine of the angle θ between the radial outward direction and the direction of the considered ray.

This is done by means of the standard tangent ray method (Hummer & Rybicki 1971; Bowers & Wilson 1991; ON98). In this scheme, the specific intensity $I_\nu(r, \mu)$ is evaluated at the external radius r_i of each shell for $1 + 2i$ values of μ.

Once $I(r_i, \mu_j)$ is known, we compute the monochromatic flux and the net outward bolometric luminosity $L(r_i)$ at each shell radius.

The cooling rate (per unit time per unit volume) of the shell i is then given by

$$\Lambda_{{\rm rad},i} = \frac{L(r_i) - L(r_{i-1})}{(4\pi/3)(r_i^3 - r_{i-1}^3)}. \tag{A10}$$

H_2 lines. To calculate the source function and the absorption coefficient, we assume LTE. This is a fair assumption, as the density is always much greater than the relevant critical values.

The absorption coefficient is given by

$$\alpha_\nu = \frac{h\nu}{4\pi}\phi(\nu)\left(\frac{2h\nu^3}{c^2}A_{21}\right)\left(n_1\frac{g_2}{g_1} - n_2\right), \tag{A11}$$

where $\phi(\nu)$ is the line profile, A_{21} is the Einstein coefficient for the relevant transition (taken from Turner et al. 1977), g_2 and g_1 are the statistical weights of the two levels involved in the transition, and n_2 and n_1 are number densities of molecules in the two considered levels, computed assuming LTE.

As noted by ON98, since the temperature typical of H_2 line emission is quite low, the line profiles are narrow and the Doppler shift caused by the gas bulk infall can be important. We assume a Gaussian profile for each line, sampled in 30 frequency bins, and we properly take into account Doppler shift in the line transfer. If the line absorption depth is <0.1, we use the optically thin approximation.

Continuum. The continuum transfer is treated as a grey problem. Again, we assume LTE to estimate the source function.

The absorption coefficient is calculated from the (Planck) opacity tables of Lenzuni et al. (1991) when $T < 7000\,\mathrm{K}$, and from the (Rosseland) opacity tables of Rogers & Iglesias (1992) for $T > 7000\,\mathrm{K}$.

As the continuum optical depth can reach values $\gg 1$ (see Fig. 8), the numerical treatment above can become inaccurate. For this reason, when $\tau > 4$ in a single shell (see the conditions listed in ON98), we use the diffusion approximation, i.e.

$$F = -\frac{16\sigma T^3}{3\alpha}\frac{\partial T}{\partial r} \simeq -\frac{16\sigma T_i^3}{3\alpha_i}\frac{T_{i+1} - T_{i-1}}{r_{i+1} - r_{i-1}}, \tag{A12}$$

where σ is the Stefan–Boltzmann constant.

APPENDIX B: LIST OF EMITTED LINES

In Table B1 we list the luminosity at infinity of each H_2 line we included in our code. Lines are sorted according to their wavelength.

The columns give, respectively:

(i) the quantum levels describing the transition;
(ii) the wavelength (in μm) of the line;
(iii) the radial optical depth from the centre of the simulated object to infinity, as evaluated at line centre, and at the epoch when the continuum optical depth is $\tau_c = 1$;

(iv) the line total luminosity at infinity, evaluated at four different epochs, i.e. when the central temperature is 650 K (L_{650}), 1000 K (L_{1000}) and 1500 K (L_{1500}), and when $\tau_c = 1$ ($L_{\tau_c=1}$); such luminosities are given in $\mathrm{erg\,s^{-1}}$;

(v) the specific luminosity (in $\mathrm{erg\,s^{-1}\,Hz^{-1}}$) at the stage when $\tau_c = 1$, estimated using a linewidth equal to the Doppler broadening $\Delta\nu = (\nu_0/c)(2kT/\mu m_H)^{1/2}$, where ν_0 is the line central frequency, $\mu \simeq 2$ is the H_2 molecular weight and T is the temperature of the shell where the radial optical depth to infinity at line centre is equal to 1 (or $T \simeq 2338\,\mathrm{K}$ for the few lines with $\tau < 1$).

The last lines of the table give the total line luminosities, the continuum luminosity and the sum of the two. The continuum luminosity is not calculated (being actually very small) when the central temperature is $\leq 1000\,\mathrm{K}$; continuum specific luminosity is only a rough estimate, since we took $\Delta\nu = \nu_{\mathrm{peak}}$, where $\nu_{\mathrm{peak}} \simeq 1.4 \times 10^{14}\,\mathrm{Hz}$ is the frequency of the peak of blackbody emission at $T = 2338\,\mathrm{K}$.

This paper has been typeset from a TEX/LATEX file prepared by the author.